

Electronic Structure of the Metal Center in the Cd²⁺, Zn²⁺, and Cu²⁺ Substituted Forms of KDO8P Synthase: Implications for Catalysis^{†,‡}

Fathima Kona,[†] Peng Tao,[†] Philip Martin, Xingjue Xu, and Domenico L. Gatti*

Department of Biochemistry and Molecular Biology, Wayne State University School of Medicine, Detroit, Michigan 48201

Received October 19, 2008; Revised Manuscript Received February 19, 2009

ABSTRACT: *Aquifex aeolicus* 3-deoxy-D-manno-octulosonate 8-phosphate synthase (KDO8PS) is active with a variety of different divalent metal ions bound in the active site. The Cd²⁺, Zn²⁺, and Cu²⁺ substituted enzymes display similar values of k_{cat} and similar dependence of K_m^{PEP} and K_m^{A5P} on both substrate and product concentrations. However, the flux-control coefficients for some of the catalytically relevant reaction steps are different in the presence of Zn²⁺ or Cu²⁺, suggesting that the type of metal bound in the active site affects the behavior of the enzyme in vivo. The type of metal also affects the rate of product release in the crystal environment. For example, the crystal structure of the Cu²⁺ enzyme incubated with phosphoenolpyruvate (PEP) and arabinose 5-phosphate (A5P) shows the formed product, 3-deoxy-D-manno-octulosonate 8-phosphate (KDO8P), still bound in the active site in its linear conformation. This observation completes our structural studies of the condensation reaction, which altogether have provided high-resolution structures for the reactants, the intermediate, and the product bound forms of KDO8PS. The crystal structures of the Cd²⁺, Zn²⁺, and Cu²⁺ substituted enzymes show four residues (Cys-11, His-185, Glu-222, and Asp-233) and a water molecule as possible metal ligands. Combined quantum mechanics/molecular mechanics (QM/MM) geometry optimizations reveal that the metal centers have a delocalized electronic structure, and that their true geometry is square pyramidal for Cd²⁺ and Zn²⁺ and distorted octahedral or distorted tetrahedral for Cu²⁺. These geometries are different from those obtained by QM optimization in the gas phase (tetrahedral for Cd²⁺ and Zn²⁺, distorted tetrahedral for Cu²⁺) and may represent conformations of the metal center that minimize the reorganization energy between the substrate-bound and product-bound states. The QM/MM calculations also show that when only PEP is bound to the enzyme the electronic structure of the metal center is optimized to prevent a wasteful reaction of PEP with water.

3-Deoxy-D-manno-octulosonate (KDO)¹ is an eight-carbon sugar present in the lipopolysaccharide (LPS) of all Gram-negative bacteria. (1) KDO provides a link between lipid A, the membrane embedded moiety of LPS, and the O-antigen, an elongated polysaccharide chain that protrudes from the bacterial outer membrane into the surrounding environment and determines the antigenic specificity of the cell. While the composition of the O-antigen varies between species and

also between strains, the inner core region containing KDO is fairly constant among all Gram-negative bacteria (2).

3-Deoxy-D-manno-octulosonate 8-phosphate synthase (KDO8P synthase, EC 4.1.2.16) plays a key role in the biosynthesis of KDO. This enzyme catalyzes the aldol-type condensation of phosphoenolpyruvate (PEP) with arabinose 5-phosphate (A5P) to form KDO8P (precursor to KDO) and inorganic phosphate (Figure 1) (3). Dephosphorylation of KDO8P to KDO and synthesis of CMP-KDO (from CTP and KDO) occur prior to the insertion of the sugar into LPS (2). Strains of *Salmonella* have been isolated with mutations in KDO8P synthase that confer temperature-sensitive growth (4, 5). Such strains fail to synthesize KDO at the nonpermissive temperature, which leads to the inhibition of the LPS biosynthesis and, as a consequence, to the arrest of cell growth. These studies indicate that KDO8P synthase provides an essential function for bacterial homeostasis and, therefore, is a potential drug target.

[†] This research was supported by U.S. Public Health Service grant GM69840 and by a Wayne State University Research Enhancement Program in Computational Biology grant to D.L.G.

[‡] The structure factor amplitudes and the refined coordinates of the Cd²⁺, Zn²⁺, and Cu²⁺ substituted forms of KDO8PS are deposited in the Protein Data Bank (entries 1FWS, 1FWW, 2A21, 2A2I, 3E0I, 3E12).

* To whom correspondence should be addressed. Phone: (313) 993-4238. Fax: (313) 577-2765. E-mail: dgatti@med.wayne.edu.

[†] These authors have contributed equally to the work.

¹ Abbreviations: KDO, 3-deoxy-D-manno-octulosonate; KDO8P, 3-deoxy-D-manno-octulosonate 8-phosphate; KDO8PS 3-deoxy-D-manno-octulosonate 8-phosphate synthase; PEP, phosphoenolpyruvate; A5P, arabinose 5-phosphate; INT, tetrahedral reaction intermediate; rmsd, root mean square deviation; L, loop; QM, quantum mechanics; MM, molecular mechanics; NBO, natural bond orbitals; NLMO, natural localized molecular orbitals; BD, bonding orbital; LP, lone pair orbital; RY, Rydberg orbital; SPY, square pyramidal; SPL, square planar; DO, distorted octahedral; DT, distorted tetrahedral; DTR, distorted trigonal; ISPY, incomplete square pyramidal.

Earlier studies have determined that the reaction of KDO8P synthesis is a sequential process in which the binding of PEP precedes the binding of A5P, and the release of inorganic phosphate precedes the release of KDO8P (6). The condensation step of the reaction is stereospecific, involving an attack by water (or a hydroxide ion) on the *si* face of C2^{PEP} and an addition of the *si* face of C3^{PEP} to the *re* face of C1^{A5P} (7–9), to form a doubly phosphorylated noncyclic

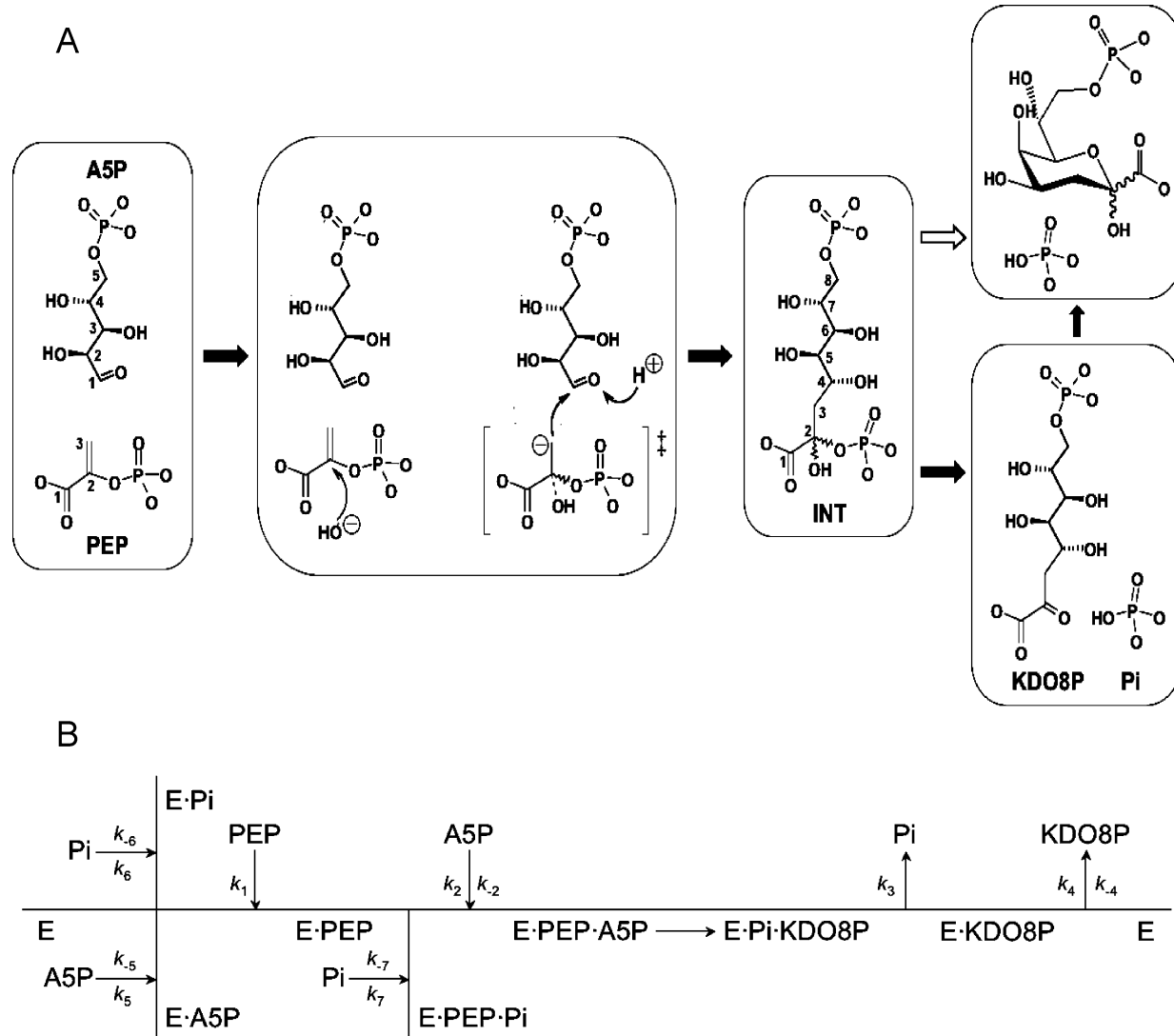


FIGURE 1: (A) Biosynthesis of KDO8P from A5P and PEP. Following or concurrent with an attack by a hydroxide ion on C2^{PEP} and protonation of the A5P carbonyl oxygen, a transient carbanion at C3^{A5P} reacts with C1^{A5P}, leading to a noncyclic tetrahedral intermediate (INT) that breaks down into KDO8P and P_i (inorganic phosphate). Transient species are in brackets and are marked with a double dagger (‡) symbol. Charges on the carboxylate and phosphate moieties are not shown. KDO8P is shown in both its linear and cyclic pyranose forms. However, direct formation of a cyclic KDO8P from an INT is unlikely (light arrow). Instead, the conversion of linear to a mixture of linear and cyclic KDO8P is expected to occur upon release of the product in solution. (B) Kinetic model of KDO8P synthesis. Noncovalent complexes are represented with dots.

intermediate that breaks down into KDO8P and inorganic phosphate (P_i) (10–13) (Figure 1). It has also been established that phosphate release occurs by cleavage of the C–O bond of PEP (9, 14) rather than the P–O bond.

The phylogenetic tree of KDO8PS is evenly divided between two forms of the enzyme characterized by the absence or presence of a metal ion in the active site (15, 16). We have reported several structures of both wild type and mutant metallo-KDO8PS from *Aquifex aeolicus* in complex with both substrates (11, 17, 18). This enzyme requires a divalent cation, with different metals (Cd²⁺, Mn²⁺, Ni²⁺, Co²⁺, Ca²⁺, Cu²⁺, Mg²⁺, and Zn²⁺), providing various levels of activity (16). Initially, we studied in detail the Cd²⁺ form of the enzyme because Cd²⁺ was reported to be the most effective activator of KDO8PS (16). In the active site of the enzyme, Cd²⁺ appears to be coordinated by the thiolate of Cys-11, the ε-nitrogen of His-185, the carboxylate moieties of Glu-222 and Asp-233 and by a water molecule. The water molecule is located on the *si* side of PEP in van der Waals

contact with the substrate C2 and C3 and is also stabilized by a hydrogen bond to the ω-nitrogen of Lys-46. Based on these observations, we have proposed that in metallo-KDO8PS it is this water that attacks C2^{PEP}. The corresponding water in nonmetallo-KDO8PSs is hydrogen bonded to an asparagine and is implicated in the formation of the reaction intermediate (13). The effects of different metals in the active site of the homologous metallo-KDO8PS from *Aquifex pyrophilus* were studied by Shulami et al. (19), and it was concluded that the binding affinities of the substrates, the rate of chemical catalysis, and the rate of product release are all affected to various extents by the type of metal bound to the active site. In this work, we set up to expand earlier knowledge about the mechanism of Cd²⁺ KDO8PS by also determining the structure and kinetic properties of *A. aeolicus* KDO8PS in complex with Zn²⁺ and Cu²⁺. Idealized coordination geometries of Cd²⁺, Zn²⁺, and Cu²⁺ in the active site of *A. aeolicus* KDO8PS were derived by a combined quantum mechanics and molecular mechanics (QM/MM)

method for the geometry optimization of the metal ligand field. Finally, the observation of the noncyclic product KDO8P bound in the active site of the Cu^{2+} substituted enzyme completed the experimental observation of all the participants (reactants, intermediates, and products) in the catalytic cycle of KDO8PS.

EXPERIMENTAL PROCEDURES

Protein Production and Purification. *A. aeolicus* KDO8PS was produced in *Escherichia coli* from plasmid pet28a/kds_a, which was derived from plasmid pet28a (Novagen) by inserting the *A. aeolicus* KDSA gene in frame with the ATG of the vector *Nco I* site, and was purified as described by Xu et al. (18). The concentrated solution of the *A. aeolicus* KDO8PS purified from *E. coli* has a pink color and a broad spectrum peak at 505 nm, likely due to bound iron. Earlier studies have shown that this enzyme contains approximately 0.4 and 0.3 equiv of Zn^{2+} and Fe^{2+} , respectively, per subunit (16). Cd^{2+} , Zn^{2+} , and Cu^{2+} substituted KDO8PS were obtained by dialyzing for 24 h the purified enzyme at the concentration of 500 μM against 20 mM Tris-Cl (pH = 7.5) containing 50 μM of Cd^{2+} , Zn^{2+} , or Cu^{2+} . We have found that this procedure gives better activities than the alternative one, consisting of dialyzing the enzyme with 5 mM EDTA prior to the addition of the metal. This is probably due to the fact that during dialysis with EDTA Cys-11 becomes partially oxidized and is no longer functional as a metal ligand (17). At the end of the substitution procedure, the Cd^{2+} and Zn^{2+} enzymes were diluted in metal-free buffer such that the final concentration of the protein was 0.5 μM and that of the free metal was 0.05 μM . The Cd^{2+} , Zn^{2+} , Co^{2+} , and Fe^{2+} contents of both the protein solution and the buffer used to dilute the protein were analyzed by inductively coupled plasma mass spectrometry (ICP-MS) on a Perkin-Elmer Elan 9000. After properly subtracting the contribution from the free metal (calculated by taking into consideration both the expected value of the free metal in the protein solution after dilution with buffer and any amount measured by ICP-MS in the buffer used to dilute the protein), the Cd^{2+} and Zn^{2+} enzymes were found to contain 1.8 and 2.7 equiv of Cd^{2+} and Zn^{2+} and less than 0.01 equiv of Fe^{2+} or Co^{2+} per subunit, respectively. At the end of the metal replacement procedure with Cu^{2+} , the enzyme acquired a greenish color, and the 505 nm peak in the spectrum was completely replaced by a new absorption peak at 380 nm. This phenomenon has been described previously by Duewel et al. (16), who have postulated that the peak is produced by a ligand-to-metal charge transfer in the Cys- Cu^{2+} adduct. Based on the reported $\epsilon_{380} \approx 3000 \text{ M}^{-1} \text{ cm}^{-1}$ for the adduct (16), the level of substitution of the original metal by Cu^{2+} was estimated to be nearly 100%.

Enzymatic Activity. Rate constants for the reaction catalyzed by KDO8PS were determined by nonlinear regression analysis (20) of the multiple progress curves of PEP consumption at 40 °C as described previously (13, 18). The curves were recorded at 232 nm ($\epsilon^{\text{PEP}} = 2840 \text{ M}^{-1} \text{ cm}^{-1}$) when the enzyme (1–2 μM) was added to a solution containing 100 mM Tris-acetate (pH = 7.5) and at several different concentrations and molar ratios of PEP, A5P, and P_i (Table 1). CdCl_2 , ZnCl_2 (50 μM), or CuCl_2 (5 μM) was added to the reaction mixture containing the enzyme. Each

Table 1: Initial Concentrations (μM) of Substrates and Products in the Reaction Progress Curves Catalyzed by the Cd^{2+} , Zn^{2+} , and Cu^{2+} KDO8PS^a

progress curve	PEP	A5P	P_i
1	96	186	0
2	100	287	0
3	192	281	0
4	142	475	0
5	270	559	0
6	412	557	0
7	184	68	0
8	293	148	0
9	377	192	0
10	472	91	0
11	375	239	0
12	428	251	0
13	553	423	0
14	455	86	600
15	486	101	900
16	98	194	300
17	99	192	600
18	466	95	2000
19	103	191	4000

^a These were used to determine the rate and kinetic constants shown in Table 2.

progress curve consisted of 100 points, for a total of 1900 points (19 curves) in each data set. The ensemble of curves was least-squares fit globally (21) with Dynafit (22) to the kinetic model shown in Figure 1B by a stepwise refinement of all the adjustable parameters. Kinetic constants under a wide range of substrate and product concentrations and flux-control coefficients for the steps of substrate binding, condensation, and product release were computed using a deterministic model with Copasi 4.4 (23). In this approach, Copasi uses the ODE solver LSODA to follow the time course defined by the differential equations that describe the model (see Supporting Information in 13) until a steady state is reached.

Structure Determination and Refinement. Crystals of *A. aeolicus* KDO8PS were obtained as described previously (11, 24) and belong to sg P3₁21. Oscillation data were collected at 100 K with an HTC image plate detector at the Cu $\text{K}\alpha$ wavelength or with a MAR-MOSAIC detector at the LS-CAT 21-ID beamline of the Advanced Photon Source (APS) and were processed with HKL (25). Structure determinations were carried out with CNS v. 1.2 or CCP4/REFMAC without NCS restraints, but with geometry restraints (using Engh and Huber expected values (26)) and isotropic thermal-factor restraints [rms (\AA^2) and σ (\AA^2) of 1.36 and 1.5 (main-chain bonds), 2.08 and 2.0 (main-chain angles), 2.08 and 2.0 (side-chain bond), 3.09 and 2.5 (side-chain angles)] using cross-validated maximum likelihood as the target function (27). As crystals of sg P3₁21 are highly isomorphous to those of the wild type, standard crystallographic refinement starting from the wild-type model was sufficient to determine each structure. In all cases, water molecules were added by means of several cycles of the automated routine for water identification available in CNS or CCP4. Each cycle of automated water addition was followed by a visual examination of the model.

QM/MM Optimization of Metal Geometries. A combined QM/MM approach (28) based on the density functional theory (DFT) was used to study KDO8PS with different metals in the active site. Prior to the QM/MM run, a complete tetramer of KDO8PS was generated from the refined

Table 2: Rate and Kinetic Constants for the Mechanistic Model of KDO8PS Shown in Figure 1^a

	Cd ²⁺ Prep 2	Cd ²⁺ (pH = 5.0) Prep 2	Cd ²⁺ Prep 1	Zn ²⁺ Prep 1	Cu ²⁺ Prep 1	Cu ²⁺ (pH = 5.0) Prep 1	Zn ^{2+/ Fe²⁺}
k_1	3.03 ± 0.06	11.19 ± 0.63	3.05 ± 0.08	1.67 ± 0.03	2.23 ± 0.02	54.1 ± 0.93	1.90 ± 0.02
$k_{-2} = k_{-2}/k_2 = K_d^{A5P-1}$	3.44 ± 0.06	1.98 ± 0.08	2.02 ± 0.06	0.04 ± 0.00	1.82 ± 0.01	23.18 ± 0.30	1.09 ± 0.04
k_3	0.61 ± 0.00	0.50 ± 0.00	0.54 ± 0.00	0.56 ± 0.00	0.50 ± 0.00	0.44 ± 0.00	0.36 ± 0.00
$k_4 = k_4/k_{-4} = K_d^{KDO8P}$	2.23 ± 0.05	5.58 ± 0.65	1.79 ± 0.05	2.89 ± 0.06	1.02 ± 0.01	1.94 ± 0.01	2.05 ± 0.02
$k_{-5} = k_{-5}/k_5 = K_d^{A5P-2}$	71.0 ± 1.00	4.58 ± 0.34	39.6 ± 1.10	29.9 ± 0.46	22.2 ± 0.31	6.74 ± 0.15	72.7 ± 2.8
$k_{-6} = k_{-6}/k_6 = K_d^{P_i-1}$	25.7 ± 0.56	36.5 ± 2.60	19.7 ± 0.53	57.2 ± 0.83	81.4 ± 0.76	21.5 ± 0.40	100 ± 2.0
$k_{-7} = k_{-7}/k_7 = K_d^{P_i-2}$	549 ± 9.9	2682 ± 210	593 ± 18	120 ± 1.3	342 ± 2.8	5770 ± 100	252 ± 8.6
k_{cat}	0.48 ± 0.03	0.46 ± 0.11	0.41 ± 0.03	0.47 ± 0.02	0.34 ± 0.01	0.36 ± 0.03	0.31 ± 0.02
K_m^{PEP}	0.16 ± 0.0	0.04 ± 0.00	0.14 ± 0.01	0.28 ± 0.01	0.15 ± 0.00	6.6e ⁻³ ± 5.4e ⁻⁴	0.16 ± 0.01
K_m^{A5P}	3.18 ± 0.17	2.27 ± 0.52	2.00 ± 0.15	0.50 ± 0.02	1.56 ± 0.04	19.26 ± 1.60	1.23 ± 0.09

^a The columns labeled Prep 1 refer to forms of KDO8PS that were derived from the same enzyme preparation. The column labeled Zn^{2+/ Fe²⁺ refers to the recombinant enzyme produced in *E. coli* and used as is without any metal substitution. This enzyme contains a mixture of Fe²⁺ and Zn²⁺ (16). The column labeled Prep 2 refers to an independent preparation of the Cd²⁺ enzyme only. All on-rate constants (k_2 , k_{-4} , k_5 , k_6 , and k_7) with the exception of k_1 were fixed at 1 s⁻¹ μM⁻¹; all other rate constants are in units of s⁻¹. All K_d 's, although numerically identical to some of the off-rate constants, are in units of μM. K_d^{A5P-1} and K_d^{A5P-2} refer to the binding of A5P to the enzyme-PEP complex and to the free enzyme, respectively. $K_d^{P_i-1}$ and $K_d^{P_i-2}$ refer to the binding of P_i to the free enzyme and to the enzyme-PEP complex, respectively. k_{cat} (s⁻¹) and K_m (μM) values were calculated according to Cleland's rules as described by Kona et al. (13) from the numerator and denominators coefficients of the rate equation derived from the rate constants by a King-Altman formalism.}

coordinates (containing only a dimer in the asymmetric unit) by the application of crystal symmetry. The ionization state of the side chains in the tetramer was determined with Molaris (29). Charges of all ionizable residues in the tetramer were then set accordingly assuming a pH = 7.0. A sphere of water molecules of 24 Å radius was generated with Molaris around the metal ion in the active site that was subjected to QM/MM optimization. Any generated water molecules closer than van der Waals distance from protein or water atoms of the original X-ray structure were removed. The entire system was relaxed with a short (10 ps, 0.001 ps stepsize) molecular dynamics run at 50 K. The rms deviation of the relaxed structure from the original crystal structure was <0.3 Å.

Spin unrestricted orbital calculations during QM/MM optimizations were carried out with Jaguar/Qsite (Jaguar, version 7.5, Schrodinger, LLC, New York, NY, 2008). The B3LYP, M06, and M06-L functionals (30–32) were used in different runs for the DFT calculations. The QM region was treated at the lacyvp* level of theory (with added + diffuse function only for the metal ion); the MM region was treated using the OPLS2005 force field (33). In one set of calculations, the entire Cys-11 and Asp-233, the side chains of Lys-41, Lys-46, His-185, Glu-222, and the metal ion, and the water molecule that appears coordinated to the metal were included in the quantum region. Three additional water molecules located within 6 Å from the metal ion were also included in the QM region, which consisted of 98 atoms in total. All atoms outside the QM region and within a sphere of 18 Å radius around the metal were included in the unrestrained MM region. The boundaries between the QM and MM regions were represented by frozen orbitals (34). All other atoms in the MM region were frozen. The optimized geometries and wave functions of the QM region were then used to perform a natural bond orbital (NBO) analysis (35) with the version of NBO 5.0 implemented inside Jaguar. As the quantum atoms cannot be used directly in NBO calculations due to the presence of frozen orbitals at the QM/MM interface, Cys-11 was truncated to ethylthiolate, His-185 was truncated to methyl-imidazole, Glu-222 and Asp-233 were truncated to propionate, and Lys-41 and Lys-46 were truncated to ethylammonium. NBO orbitals were visualized with NBOView 1.0.

In a second set of calculations, Cys-11, Lys-41, Lys-46, Arg-49, Lys-124, Arg-154, His-185, Glu-222, Asp-233, Arg-106 of another subunit, the metal ion, KDO8P, and P_i were included in the quantum region. To avoid the very large increase in the number of quantum atoms that would derive from the inclusion in these calculations of the additional ligands (KDO8P, P_i) and of the side chains (Lys or Arg) required to neutralize the charges carried by these ligands, the boundaries between the QM and MM regions were represented by link hydrogen atoms (36) placed between CA and CB for Cys and Asp, between CB and CG for Glu and His, between CG and CD for Arg, and between CD and CE for Lys. By means of this strategy, the total number of quantum atoms was kept at 118–120. All atoms outside the QM region and within 10 Å of any residues containing quantum atoms were included in the unrestrained MM region. All other atoms in the MM region were frozen.

RESULTS AND DISCUSSION

Enzymatic Activity of Cd²⁺, Cu²⁺, and Zn²⁺ Substituted KDO8PS. A mechanistic model of KDO8P synthesis that fits well with both kinetic and crystallographic studies has been described previously (13, 18) (Figure 1B). This model was shown to be particularly effective in the simulation of experimental progress curves. Typically, no significant differences were observed in the magnitude of the residual between the experimental and the best-fit progress curves whether both the on- and off-rate constants were refined or only the off-rate constants. However, smaller standard errors of the refined variables were obtained when all second-order rate constants were fixed at 10⁶ s⁻¹M⁻¹. Rate constants for the different components of the kinetic model shown in Figure 1B are listed in Table 2 for recombinant KDO8PS as purified upon production in *E. coli* (column labeled Zn^{2+/ Fe²⁺) or upon substitution of the native metal with Cd²⁺, Zn²⁺, or Cu²⁺. With the exception of the columns labeled Prep 2 (a preparation of the Cd²⁺ enzyme only), all the rate constants of Table 2 were obtained with a single preparation of KDO8PS (Prep 1) used as is or as variably substituted at the metal site. Results obtained with two different preparations of the Cd²⁺ enzyme are shown here to attest to the very good reproducibility of both the metal replacement}

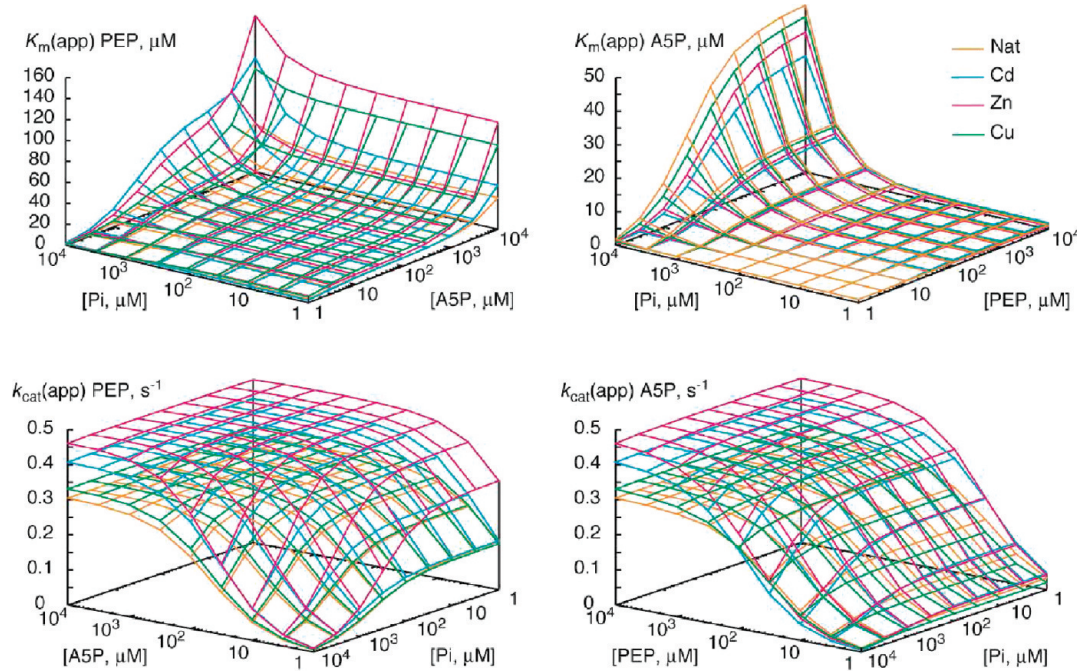


FIGURE 2: Apparent K_m and k_{cat} of metal-substituted KDO8PS in the presence of different concentrations of reactants (PEP or A5P) and products (KDO8P or P_i). Only surfaces corresponding to a concentration of 100 μM KDO8P are shown.

procedure and the kinetic analysis. All subsequent analyses refer, however, to the results obtained with the forms of KDO8PS that, although having different metals in the active site, were derived from a single enzyme preparation (Prep 1). Table 2 includes also a kinetic analysis of the Cd^{2+} (Prep 2) and Cu^{2+} (Prep 1) enzymes at pH = 5.0; the mechanistic relevance of these additional data is discussed later on.

In our previous work, an initial rate equation for the simplified steady-state kinetic model, corresponding to the full numerical model used in the regression analyses, was derived by application of the King–Altman method (37–39). Kinetic constants were calculated by substituting the best-fit values of the rate constants from the full numerical model into the rate equation according to Cleland's rules (40), which define k_{cat} , K_m 's, and K_i 's as ratios between different coefficients in the rate equation. However, as pointed out by Segel in *Enzyme Kinetics* (38), this approach is theoretically unsatisfactory in the most general case of multisubstrate kinetics and it also fails to capture visually the dependence of the apparent k_{cat} 's and K_m 's on the concentrations of the inhibiting substrate (A5P) and products (KDO8P and P_i) that might occur in vivo. For this reason in this work, knowledge of the rate constants for all the steps of the reaction was used to simulate the enzyme behavior under a wide variety of conditions that might occur inside the cell. We used the metabolic simulator Copasi (23) to compute a 4-D matrix of the steady-state rates of the KDO8P formation attained when the enzyme operates under a wide range (1 μM –10 mM reactants and products) of metabolic conditions. The original 4-D matrix was then decomposed with an ad hoc program into separate sets of 3-D matrices suitable for plotting, describing the dependence of the apparent values of $k_{\text{cat}}^{\text{PEP}}$, $k_{\text{cat}}^{\text{A5P}}$, K_m^{PEP} , and K_m^{A5P} on the concentration of the scanned parameters.

The results of this analysis are shown as contour surfaces in Figure 2. The nodal points of the contour surfaces of the bottom panels represent steady-state values of the flux

$J(\text{KDO8P}) (\mu\text{M} \cdot \text{Volume} \cdot \text{s}^{-1})$ through the product release step ($\text{E} \cdot \text{KDO8P} \rightleftharpoons \text{E} + \text{KDO8P}$), calculated under conditions in which the concentrations of PEP, A5P, P_i , and KDO8P (also all of the free and bound enzyme species) remain constant over time (true steady state). In all cases, the sum of the concentrations of all the enzyme species is 0.1 μM . In the bottom-left panel, each node represents the largest observed value of the flux $J(\text{KDO8P})$ at a fixed concentration of A5P, P_i , and KDO8P, while cycling from 1 μM to 10 mM PEP. Thus, upon dividing the flux values by the amount of enzyme present, each node represents an apparent k_{cat} with respect to PEP. In the bottom-right panel, each node represents the largest observed value of the flux $J(\text{KDO8P})$ at a fixed concentration of PEP, P_i , and KDO8P, while cycling from 1 μM to 10 mM A5P. Thus, upon dividing the flux values by the amount of enzyme present, each node represents an apparent k_{cat} with respect to A5P. In the contour surfaces of the two top panels each node represents a concentration of substrate at which half of the maximum steady-state value of the flux $J(\text{KDO8P})$ is attained and is an apparent K_m (for PEP or A5P). Altogether, the contour surfaces (as 9 \times 9 grids) contain the same information as 81 separate steady-state kinetic analyses for PEP and 81 for A5P, providing a comprehensive view of the enzyme behavior under different metabolic states. It is worth noting that a wealth of additional information is contained in the 4-D matrix: in fact, as the KDO8P concentration is unlikely to exceed 100 μM in the bacterial cytosol, only the contour surfaces corresponding to the steady states attained at 100 μM KDO8P are shown. Contour surfaces for a full range of concentrations from 1 μM to 10 mM KDO8P were extracted from the original 4-D matrix, but are not shown here for brevity.

The top-left panel of Figure 2 shows a large plateau between 1 μM and \sim 1 mM A5P and P_i in which the apparent K_m^{PEP} remains below 20 μM . At higher concentrations of A5P and P_i , competition with respect to PEP for the binding

to free enzyme becomes evident. The top-right panel shows a plateau between 1 μM and $\sim 1 \text{ mM}$ P_i and 1 μM and 10 mM PEP in which the apparent K_m^{A5P} remains below 5 μM . At higher concentrations of P_i , competition with respect to A5P for the binding to the E·PEP complex becomes evident. The bottom panels show that the Zn^{2+} enzyme has the highest activity, followed by the Cd^{2+} and Cu^{2+} enzyme, with the unsubstituted enzyme (Nat) being the least active. Whether the apparent k_{cat} is measured with respect to PEP or A5P, it decreases (as expected) at lower concentrations of the other substrate and with increasing concentrations of P_i . At low A5P concentration (1–10 μM), the Zn^{2+} enzyme is twice as active as the other enzymes in the 1–100 μM range of P_i .

The merit of computing a 4-D metabolic matrix can be recognized by observing that, in view of the cost of A5P, a determination of $k_{\text{cat}}^{\text{PEP}}$ by initial velocities studies would likely be carried out at a concentration of A5P of ~ 50 –100 μM (20–40 times the K_m^{A5P}), and would underestimate the maximum apparent value of $k_{\text{cat}}^{\text{PEP}}$ (bottom left panel of Figure 2). It is also notable that the maximum value of $k_{\text{cat}}(\text{app})$ and the minimum value of $K_m(\text{app})$ obtained from the 4-D matrix correspond well to the k_{cat} and K_m values derived by application of the King–Altman method and Cleland's rules (Table 2).

Altogether this analysis shows that, despite individual quantitative differences, the four types of metal KDO8PS's are qualitatively similar. However, a different approach based on the principles of metabolic control analysis (MCA) (41–43) shows some important differences. In MCA, one studies the relative control exerted by each step on the system's variables (e.g., fluxes and species concentrations). This control is measured by applying a perturbation to the step being studied and then by measuring the effect on the variable of interest after the system has settled to a new steady state. A control coefficient is defined as the relative measure of how much a perturbation on a parameter affects a system variable (e.g., fluxes or concentrations) (42):

$$C_{v_i}^A = (\partial A / \partial v_i)(v_i / A)$$

where A is the variable, i the step, and v the steady-state rate of the perturbed step. The most common control coefficients are those for fluxes and species concentrations, but any variable of the system can be analyzed with MCA and have control coefficients defined by analogous equations. A very important property of steady-state metabolic systems concerns the summation of all the flux-control coefficients: it can be demonstrated (42) that for any given flux the sum of the flux-control coefficients of all steps is equal to unity:

$$\sum_i C_{v_i}^J = 1$$

According to this summation theorem, an increase in some of the flux-control coefficients implies that others decrease. Therefore, control coefficients are global properties, and metabolic control is a systemic property dependent on all of the system's elements (or steps). This result challenges the view that a single step of an enzymatic reaction is rate limiting, and that the rate-limiting step is always the same, regardless of the global metabolic conditions (steady-state values of substrates and products). We have used the

metabolic simulator Copasi to determine the control coefficients of each of the four catalytically relevant steps of the reaction ($E \rightleftharpoons E \cdot \text{PEP} \rightleftharpoons E \cdot \text{PEP} \cdot \text{A5P} \rightleftharpoons E \cdot \text{KDO8P} \rightleftharpoons E$) on the overall flux J ($\mu\text{M Volume s}^{-1}$) through the four steps under steady-state conditions, corresponding to fixed concentrations of P_i (10 mM) and KDO8P (100 μM) and concentrations of PEP and A5P ranging from 1 μM to 1 mM . These values for the parameter scan were chosen to reflect the likely concentrations of substrates and products in vivo (44, 45). The result of this analysis is shown as contour surfaces in the panels of Figure 3.

The top-left panel shows a plateau (common to all metal forms) in the concentration range of 30 μM –1 mM A5P, 1–10 μM PEP in which overall flux J is controlled almost exclusively by the binding of PEP to the free enzyme [first reaction step (R1), $E + \text{PEP} \rightleftharpoons E \cdot \text{PEP}$]. The top-right panel shows that in the native, Cd^{2+} and Cu^{2+} enzymes binding of A5P [second reaction step (R2), $E \cdot \text{PEP} + \text{A5P} \rightleftharpoons E \cdot \text{PEP} \cdot \text{A5P}$] has only a modest control on the reaction ($\text{Cc}(J)\text{R2} \leq 0.2$). In contrast in the Zn^{2+} enzyme, there is a plateau in the concentration range of 1–100 μM PEP and 1–10 μM A5P in which overall flux is controlled almost exclusively by the binding of A5P to the E·PEP complex. In the native, Cd^{2+} and Cu^{2+} enzymes the condensation step of the reaction (R3, $E \cdot \text{PEP} \cdot \text{A5P} \rightleftharpoons E \cdot \text{KDO8P} + \text{P}_i$) is the predominant factor controlling flux in the concentration range 100 μM –1 mM PEP, regardless of the concentration of A5P. In contrast, in the Zn^{2+} enzyme this step exerts significant control on the reaction only at the highest concentrations of both PEP and A5P. Finally, all metal forms of the enzyme show qualitatively similar flux control by the product release step ($E \cdot \text{KDO8P} \rightleftharpoons E + \text{KDO8P}$), which becomes a significant factor only at the highest concentrations of both PEP and A5P: the Cu^{2+} enzyme appears to be most sensitive to this step with a $\text{Cc}(J)\text{R4}$ value almost double that of the native or the Zn^{2+} enzymes. Altogether, the observed $\text{Cc}(J)$ profiles suggest that flux control in vivo in the Zn^{2+} enzyme is quite different from that of the other metal forms.

Structure of Zn^{2+} and Cu^{2+} KDO8PS. Structures of Zn^{2+} and Cu^{2+} KDO8PS were determined after soaking crystals overnight with 0.5 mM PEP and 0.5 mM PEP + 1.0 mM A5P. Crystals belong to space group $P3_121$, $a = b \approx 84 \text{ \AA}$, $c \approx 160 \text{ \AA}$ (Table 3) and contain a dimer (half of the tetrameric enzyme) in the asymmetric unit. The overall features of Zn^{2+} and Cu^{2+} KDO8PS are very similar to those of the Cd^{2+} enzyme that were reported previously (11); thus, we are primarily interested in differences around the metal. With regard to this point, it is important to notice that although the ICP-MS analysis indicated the presence of 1.8 and 2.7 equiv of Cd^{2+} and Zn^{2+} per subunit, only one metal site per chain was identified in the crystal structure. The metal centers of KDO8PS in complex with PEP in the three metal forms are shown in Figure 4. All three sites display a potential octahedral coordination with Cys-11, His-185, Glu-222 (bidentate), Asp-233, and a water molecule located on the *si* side of PEP as ligands. The Cd^{2+} and Zn^{2+} sites are essentially identical, while the Cu^{2+} site is asymmetrically distorted with Cys-11 and His-185 closer to the metal and Glu-222, Asp-233, and water more distant from it (Figure 4C). In this latter structure the Jahn–Teller instability (46) of the octahedral geometry for Cu^{2+} (d^9) is resolved through a shortening (as found, for example, in the K_2CuF_4 complex)

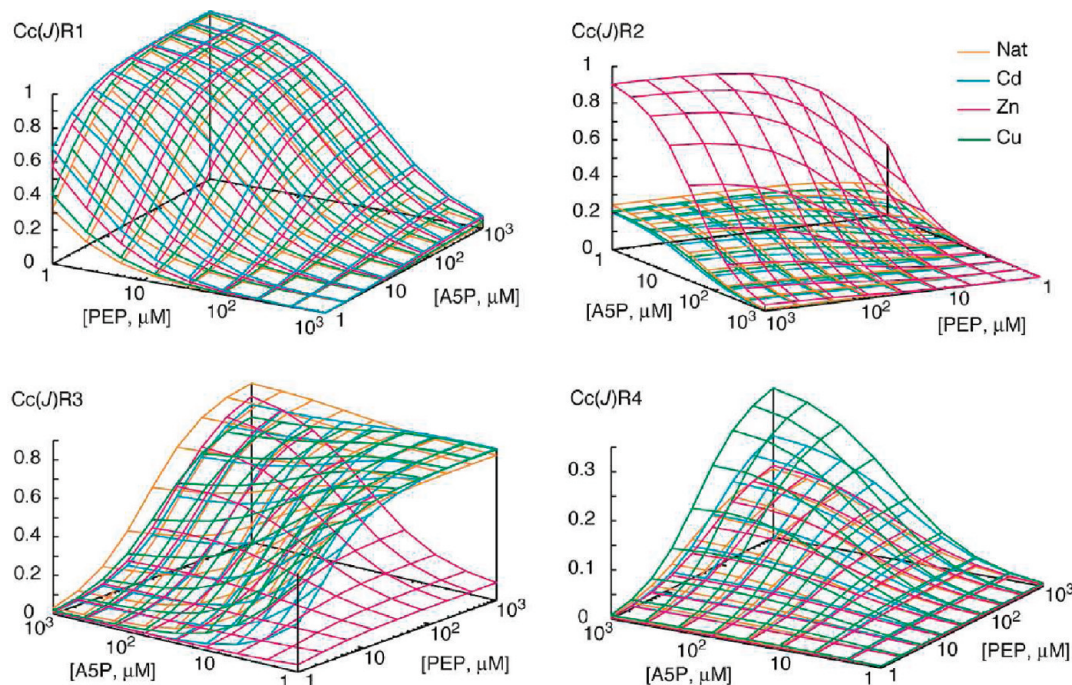


FIGURE 3: Flux control coefficients $Cc(J)$ for reaction steps R1 ($E + PEP \rightleftharpoons E \cdot PEP$), R2 ($E \cdot PEP + A5P \rightleftharpoons E \cdot PEP \cdot A5P$), R3 ($E \cdot PEP \cdot A5P \rightarrow E \cdot KDO8P + P_i$), and R4 ($E \cdot KDO8P \rightleftharpoons E + KDO8P$) under steady-state conditions, corresponding to fixed concentrations of P_i (10 mM) and KDO8P (100 μM).

of the trans bonds on the z -axis with respect to the bonds on the xy square plane, rather than the more common lengthening of such bonds in a tetragonal distortion (see (47)).

Three different metal environments (Figure 5) are produced when crystals of Cd^{2+} , Zn^{2+} , and Cu^{2+} KDO8PS are soaked in the presence of both PEP and A5P. In all three cases the metal displays a potential octahedral coordination with Cys-11, His-185, Glu-222, and Asp-233 and with the final ligand provided by water in the Cd^{2+} enzyme, by $C2-OH^{A5P}$ in the Zn^{2+} enzyme, and by $C4-OH^{KDO8P}$ in the Cu^{2+} enzyme. The overall geometry of the metal center is very similar in the Cd^{2+} and Zn^{2+} enzyme, while the Cu^{2+} site is asymmetrically distorted with the axial ligands Cys-11 and His-185 closer to the metal, and the remaining equatorial ligands farther apart from it, as already seen in the structures with PEP bound.

The Cu^{2+} structure provides for the first time a direct view of the products KDO8P (in its noncyclic form) and P_i bound in the active site of a metallo-KDO8PS (Figures 5C,D and 6), as they would appear at the end of the condensation reaction prior to their release in solution. This finding provides complementary information to the observation by Vainer et al. (48) of how KDO8P (in its cyclic form) would rebind to the enzyme from solution, thus acting as an inhibitor. Consistent with the kinetic model shown in Figure 1, which indicates that P_i is released before KDO8P, the refined occupancy of phosphate in the active site of Cu^{2+} KDO8PS is ~0.6 (with $\langle B \rangle = 26.7 \text{ Å}^2$), while that of KDO8P is ~0.9 (with $\langle B \rangle = 22.6 \text{ Å}^2$).

In previous reports, we have suggested that a mechanism of alternating site catalysis might be operational in *A. aeolicus* KDO8P synthase (11). This proposal was based on the observation that in the Cd^{2+} enzyme A5P binds only to one of the two active sites of the dimer contained in the asymmetric unit of the crystal. Application of crystal symmetry to generate the tetramer reveals that the binding

of A5P occurs at the active sites located on only one of the two faces of the enzyme. When A5P binds simultaneously with PEP, the associated ordering of the L7 loop, which seals the cavity of the active site, also takes place only on one face of the enzyme. A key role in establishing the enzyme asymmetry is played by the metal. If Cd^{2+} is present, a change in conformation appears to originate in the active sites located on one face of the enzyme, that prevents binding of A5P in the active sites located on the opposite face. However, in the absence of metal, information on the occupancy of the active sites of one face is no longer transferred to the other face. The consequence of this lack of communication is that the active sites on both faces of the enzyme act independently and bind A5P simultaneously (11). In consideration of the symmetry breaking effects of Cd^{2+} on the structure of the enzyme active sites, it was of interest to determine whether other metals also produce the same effects. In the Zn^{2+} enzyme, PEP and A5P bind in both active sites, but the L7 loop is ordered only in one of them. In the Cu^{2+} enzyme, KDO8P and P_i bind in both active sites and in both cases the L7 loop is disordered, as expected from the fact that P_i is already leaving the enzyme (see above). Thus, it appears that the structural asymmetry between different active sites, which is characteristic of the Cd^{2+} enzyme, is mostly lost in the Zn^{2+} and Cu^{2+} enzymes.

QM/MM Simulations of the Metal Centers in Cd^{2+} , Zn^{2+} , and Cu^{2+} KDO8PS. As molecular mechanics (MM) restraints are included in the refinement of protein X-ray structures at medium-high resolution, the quality of the final structures depends also on the quality of the MM potentials. While very accurate force fields are available for amino acids and nucleic acids, there are no accurate force fields for metals, and metal centers are typically treated without MM restraints during crystallographic refinement. This usually means that no explicit bonds are defined between the metal and its ligands, and only van der Waals and Coulomb terms are

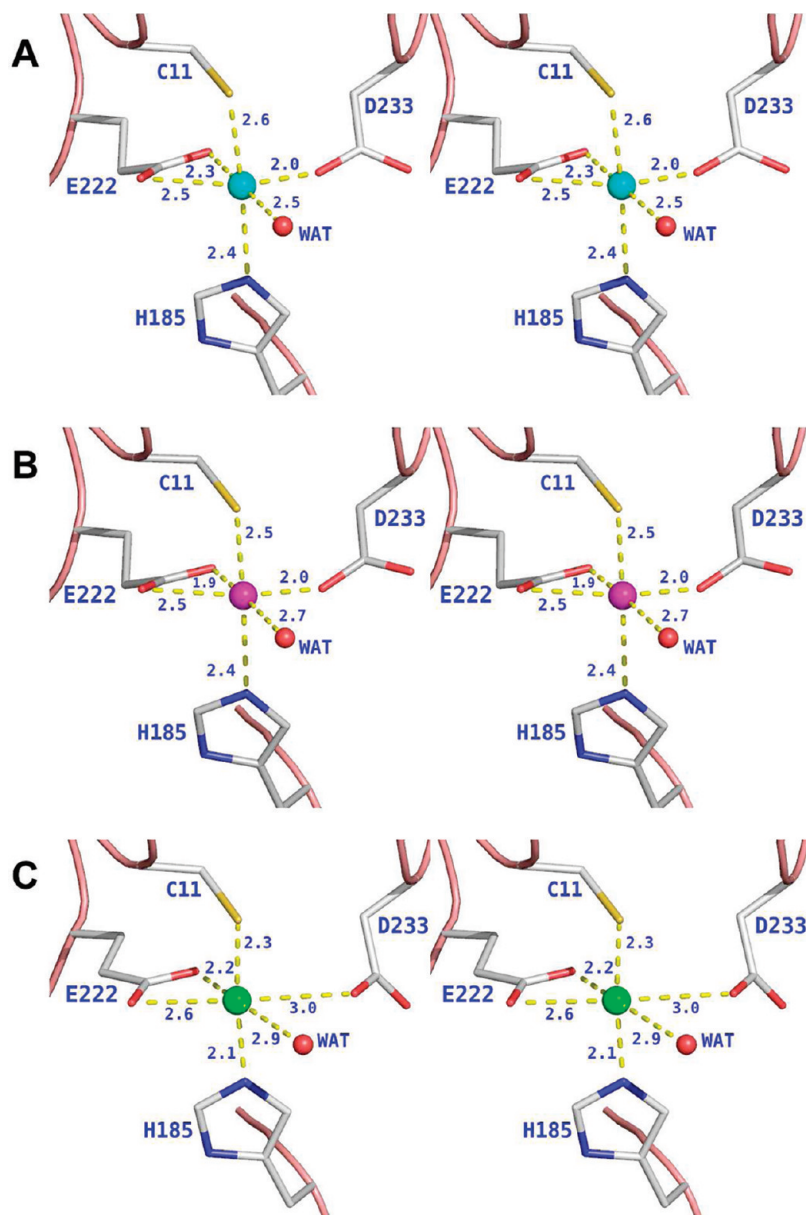


FIGURE 4: Metal coordination in KDO8PS incubated with PEP. (A) Cd²⁺ KDO8PS with bound PEP. (B) Zn²⁺ KDO8PS with bound PEP. (C) Cu²⁺ KDO8PS with bound PEP. In these three panels the metal is shown as a sphere colored cyan (Cd²⁺), magenta (Zn²⁺), and green (Cu²⁺), respectively. Predicted metal bonds are shown as yellow dashed lines with the bond length in Å.

included. As these interactions tend to reach energy minima away from molecular bonds, the real metal–ligand distances can be somewhat different from the values observed in the crystal structures. A solution to this problem is to replace the inaccurate MM potentials with highly accurate quantum mechanical (QM) calculations for the small part of the protein that contains the metal site. While at least one package for combined QM/MM refinement of proteins has been developed (ComQum-X (49)), it is not yet generally available. As an alternative, we have used the refined crystal structures of metal-substituted forms of KDO8PS in complex with PEP or KDO8P as the starting points for a QM/MM geometry optimization of the metal centers (see Table 3 and Experimental Procedures). Another important reason for pursuing this approach is that analysis of the wave function associated with the QM/MM optimized geometry provides a detailed description of the electronic structure of the metal centers,

which otherwise can only be guessed from even the most accurate metal–ligand distances and geometries.

An accurate QM representation of the metal centers also requires knowledge of the ionization state of the metal ligands. We have used the program Molaris (29) to determine the protonation state of the ionizable residues in KDO8PS, and based on this analysis it was inferred that the amino acid side chains that coordinate the metal are deprotonated at pH = 7.0 (Table 4). However, it must be stressed that the determination of protein pK_a's by computational means is still controversial (50, 51), and that significant pK_a shifts in buried residues can be overlooked by current methods. In the case of the KDO8PS metal center, the problem is compounded by the fact that the metal is both shielding the ligands from solvent and shifting their pK_a directly by virtue of its double positive charge. For this reason, in order to achieve an accurate QM representation of the metal centers

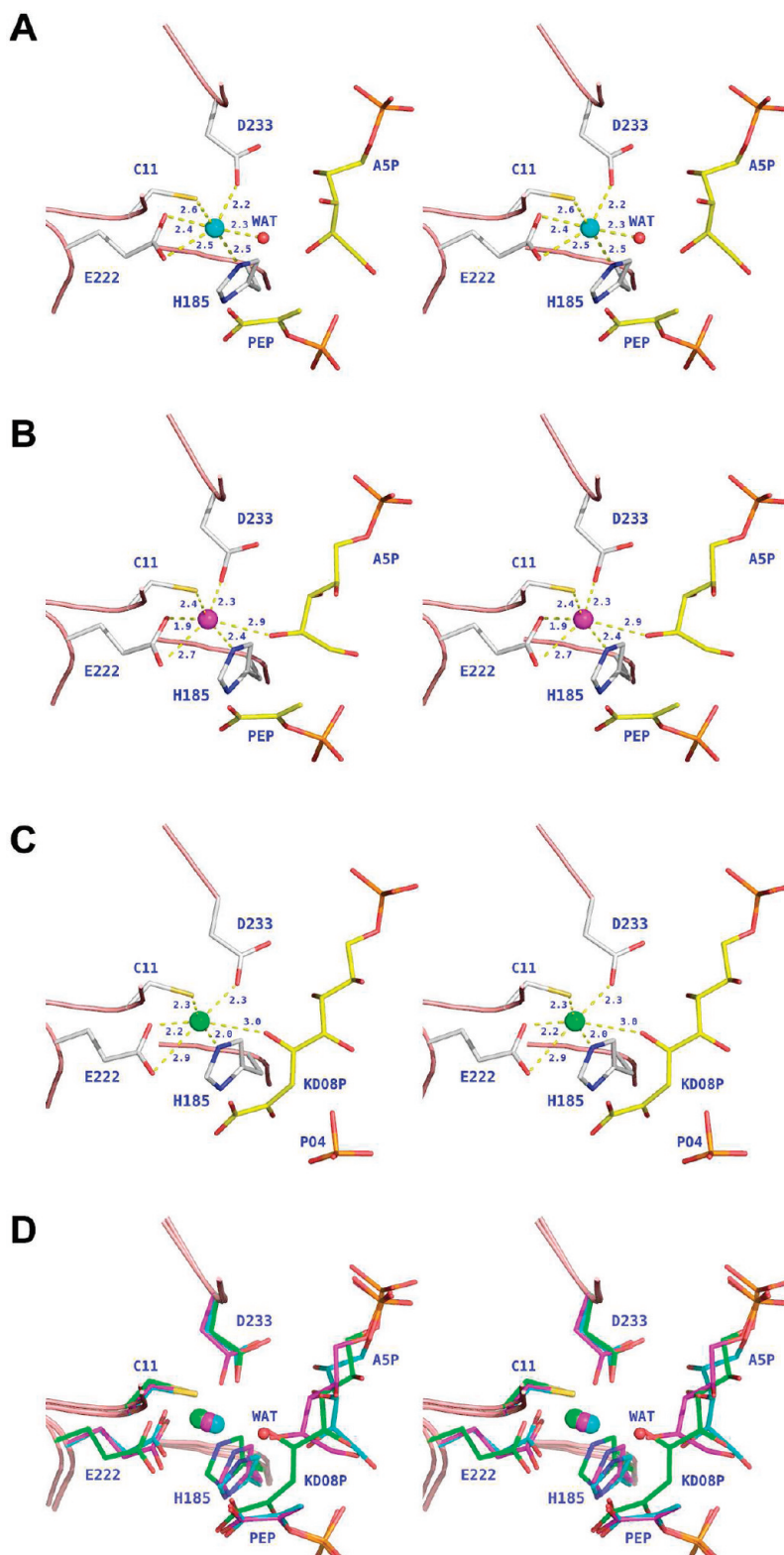


FIGURE 5: Metal coordination in KDO8PS incubated with PEP and A5P. (A) Cd^{2+} KDO8PS with bound PEP and A5P. (B) Zn^{2+} KDO8PS with bound PEP and A5P. (C) Cu^{2+} KDO8PS; PEP and A5P have reacted forming KDO8P and Pi . In these three panels the metal is shown as a sphere colored cyan (Cd^{2+}), magenta (Zn^{2+}), and green (Cu^{2+}), respectively. Predicted metal bonds are shown as yellow dashed lines with the bond length in Å. (D) Superposition of the active sites of Cd^{2+} KDO8PS (cyan bonds), Zn^{2+} KDO8PS (magenta bonds), and Cu^{2+} KDO8PS (green bonds) incubated with PEP and A5P. The metal is shown as a sphere colored cyan, magenta, and green, respectively, as in the top three panels. There is still a water molecule in the coordination sphere of the metal in Cd^{2+} KDO8PS, which is replaced by $\text{C}_2\text{-OH}^{\text{A5P}}$ in Zn^{2+} KDO8PS, and by $\text{C}_4\text{-OH}^{\text{KDO8P}}$ in Cu^{2+} KDO8PS.

the geometry optimization was carried out in the presence of all possible ionization states of the coordinating side chains. With regard to this point, it is important to notice

that four different protonation configurations were recognized as possible for each of the side chains of Glu-222 and Asp-233, depending on which oxygen atom in the carboxylate

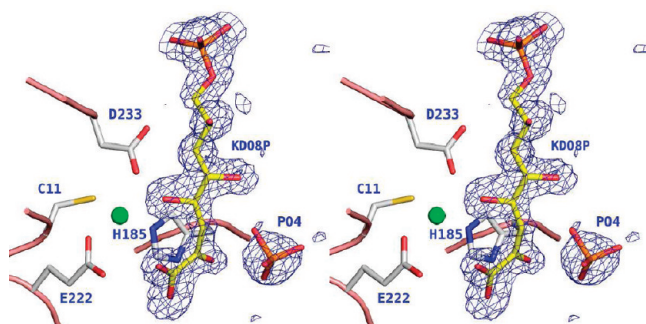


FIGURE 6: Detail of the active site of Cu^{2+} -KDO8PS with an $|F_0 - F_c| \sigma_A$ omit map contoured at 3σ around KDO8P (yellow bonds) and P_i (orange bonds).

group accepts the proton (OE1, OE2, OD1, OD2), and on the direction of this proton, for which two energy minima exist separated by a 180° rotation around the C–O bond (Figure 7). In each of these configurations a different, but equally plausible, network of hydrogen bonds propagates from the metal center outward; therefore, each state must be considered as potentially occurring in the protein. Thus, a total of 11 different ionization states (one with all the ligands deprotonated, one for protonated Cys-11 with the proton pointing away from the metal, one for protonated His-185, and four each for protonated Glu-222 and Asp233) were tested by QM/MM for each of the three metal forms of KDO8PS under examination.

Another important issue is the choice of quantum method. The most widely used method to describe electronic structures is the density functional theory (DFT), (52, 53) with B3LYP (30, 31) being probably the most popular functional, even in the context of transition metal chemistry (54, 55). In its basic form, B3LYP is a correlation-exchange functional

whose exchange component is partly the local Slater–Dirac exchange, partly the exact Hartree–Fock (HF) exchange (at 20% level), and partly the Becke 88 exchange functional (56), which is why it is termed a hybrid functional. The correlation component is calculated in part (0.19) from the VWN-5 functional (57) and in part (0.81) from the LYP functional (58). Although B3LYP is widely used, its performance is still unsatisfactory with respect to the determination of barrier heights (usually underestimated), noncovalent interactions (inaccurate description of van der Waals complexes in the 2–5 Å range), and even transition metal chemistry, in which better performance has often been obtained with B3LYP variants with reduced HF exchange (e.g., B3LYP* with 15% HF exchange (59)), or with local functionals (0% HF exchange) (60). With regard to transition metals, there is also evidence that B3LYP (and other hybrid functionals) overestimates bond lengths, underestimates bond dissociation energies, and tends to give larger dipole moments, thus overestimating the ionic versus covalent character of bonds (55). Some of these problems have been addressed in the development of the M06 suite of density functionals (32), which was shown to perform comparably or better than B3LYP in a number of test cases not included in the databases used to train the functionals. While most of our calculations were performed with B3LYP, some were repeated also with the M06 functional (27% HF exchange) and with the nonhybrid gradient-corrected functional M06-L (0% HF exchange), thus providing also a benchmark for the effect of different amounts of HF exchange in the functional on the final optimized geometries and the associated wave functions. Finally, all calculations were performed with the lacvp* basis set (lacvp⁺* for the metals). In this basis set all atoms H through Ar are described with 6-31G*, while heavier

Table 3: X-ray Data Collection and Refinement Statistics^a

	$\text{Zn}^{2+} + \text{PEP}$	$\text{Zn}^{2+} + \text{PEP} + \text{A5P}$	$\text{Cu}^{2+} + \text{PEP}$	$\text{Cu}^{2+} + \text{KDO8P}$
Data Collection				
wavelength	Cu K α	Cu K α	1.0 Å (APS)	1.0 Å (APS)
space group	$P\bar{3},21$	$P\bar{3},21$	$P\bar{3},21$	$P\bar{3},21$
resolution (Å)	41–1.8 (19–1.8)	26–1.95 (2.0–1.95)	21–1.68 (1.8–1.68)	22–1.7 (1.79–1.7)
unique reflections	57 525 (7257)	46 274 (2742)	72 792 (8192)	73 254 (10 084)
$\langle \text{redundancy} \rangle$	7.9 (2.8)	11.5 (3.7)	21.6 (18.9)	21.2 (18.3)
completeness (%)	93.2 (78.9)	94.8 (57.1)	96.1 (74.9)	98.9 (94.7)
$\langle I \rangle / \sigma \langle I \rangle$	10.7 (2.0)	26.4 (1.74)	26.5 (7.7)	23.6 (5.4)
R_{merge}^b (%)	9.9 (37.8)	7.6 (58.9)	9.0 (30.4)	10.6 (42.6)
Refinement				
program	CNS	CNS	REFMAC	REFMAC
PDB entry	2A21	2A21	3E01	3E12
R_{cryst}^c (%)	18.4 (26.2)	19.5 (32.9)	16.2 (24.7)	16.7 (27.9)
R_{free} (%)	21.0 (27.7)	22.9 (35.0)	18.5 (28.6)	19.6 (28.1)
amino acids	517	525	517	525
water	550	261	565	545
$\langle B^{\text{overall}} \rangle$ (Å 2)	31.5	46.6	21.6	21.6
$\langle B^{\text{protein/water}} \rangle$ (Å 2)	29.6/44.8	46.1/49.9	19.5/35.4	19.6/35.2
$\langle B^{\text{metal}} \rangle$ (Å 2)	36.3	57.5	19.2	16.4
$\langle B^{\text{PEP/A5P}} \rangle$ (Å 2)	24.9	50.3/74.4	15.6	
$\langle B^{\text{KDO8P/P}_i} \rangle$ (Å 2)				22.6/26.7
coordinate error (Å)	0.20	0.28	0.10	0.10
rmsd bonds (Å)	0.005	0.006	0.014	0.014
rmsd bond angles	1.3	1.3	1.4	1.5
rmsd dihedrals	22.40	22.8	18.5	17.1

^a KDO8PS crystals were soaked overnight in the presence of 0.5 mM PEP or 0.5 mM PEP + 1 mM A5P. Upon data collection and refinement, KDO8P was found in the active site of the crystal of Cu^{2+} -KDO8PS incubated with PEP + A5P. Each data set was collected from a single crystal at 100 K. ^b $R_{\text{merge}} = \sum_i \sum_j I(h)_i - \langle I(h) \rangle / \sum_i \sum_j I(h)_i$, where $I(h)_i$ is the i th measurement. ^c $R_{\text{cryst}} = \sum |F_{\text{obs}} - F_{\text{calcd}}| / \sum |F_{\text{obs}}|$. R_{free} was calculated on 10% of the data omitted from refinement. The coordinate error was derived from a cross-validated Luzzati plot. Values in parentheses refer to the highest resolution shell.

Table 4: Apparent pK_a 's of the Side Chains Included in the QM Region during the QM/MM Optimization of the Metal Center of Cd^{2+} , Zn^{2+} , and Cu^{2+} KDO8PS^a

	$\text{Cd}^{2+} + \text{PEP}$	$\text{Zn}^{2+} + \text{PEP}$	$\text{Cu}^{2+} + \text{PEP}$	$\text{Cd}^{2+} + \text{PEP} + \text{A5P}$	$\text{Zn}^{2+} + \text{PEP} + \text{A5P}$	$\text{Cu}^{2+} + \text{KDO8P}$	$\langle pK_a \rangle, \sigma$
Cys-11	4.0	0.9	1.7	6.1	2.7	1.4	2.8, 1.8
His-185	5.2	4.5	8.5	2.9	8.2	8.4	6.3, 2.2
Glu-222	2.3	2.4	-5.4	2.6	-3.5	-3.9	-0.9, 3.1
Asp-233	-4.1	-3.5	-1.7	-4.2	-2.6	-5.0	-3.5, 1.1

^a pK_a values were calculated from the X-ray structures of the enzyme in complex with PEP, PEP + A5P, or KDO8P, respectively. Each value represents the average of the values determined for the two chains of KDO8PS contained in the asymmetric unit of the crystals.

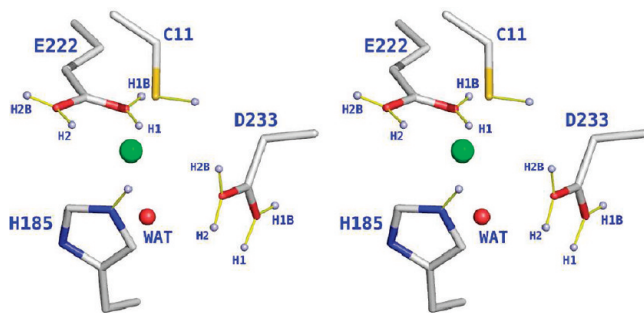


FIGURE 7: Ionization states of KDO8PS explored by QM/MM. Small light-blue spheres connected to the heavy atoms by yellow lines indicate the possible positions of protons (H_1 and $\text{H}_{1\text{B}}$ for $\text{OD}_1^{\text{D}233}$ or $\text{OE}_1^{\text{E}222}$, H_2 and $\text{H}_{2\text{B}}$ for $\text{OD}_2^{\text{D}233}$ or $\text{OE}_2^{\text{E}222}$) in the ionization states of residues included in the QM region (see Table 5).

atoms (e.g., Cu, Zn, and Cd) are modeled using the LANL2DZ effective core potentials basis set.

Ionization State of the Metal Ligands in Cd^{2+} , Zn^{2+} , and Cu^{2+} KDO8PS. Table 5 gives an overview of the deviation of the QM/MM optimized geometries of the metal centers (in the 11 ionization states mentioned above) from the experimental ones. The rms deviations were calculated between the vectors (one for the X-ray structure and one for the QM/MM structure) containing the unique elements (21 in total) of the distance matrix relating the metal and its ligands (Me^{2+} , $\text{SG}^{\text{C}11}$, $\text{NE}2^{\text{H}185}$, $\text{OE}1^{\text{E}222}$, $\text{OE}2^{\text{E}222}$, $\text{OD}2^{\text{D}233}$, and O^{WAT}) or between the vectors (one for the X-ray structure and one for the QM/MM structure) containing the angles that uniquely describe the geometry of the metal center (15 in total, each one defined by the metal and two ligands). Different ionization states were mostly tested with B3LYP, but those that identify particularly good fits to the experimental structures were repeated also with M06 and M06-L. For Cd^{2+} , the best fit to the experimental geometry is observed when Asp-233 is protonated at the oxygen not involved in coordinating the metal ($\text{OD}_1-\text{H}_1\text{B}$, Figure 7). However, a Cd^{2+} metal center with fully deprotonated ligands is a very close second best match. For Zn^{2+} , the best fit is observed when all ligands are deprotonated, and the second best when Asp-233 is protonated at the oxygen not involved in coordinating the metal ($\text{OD}_1-\text{H}_1\text{B}$, Figure 7). For Cu^{2+} , the best results are obtained when Asp-233 is protonated at either one of its oxygens ($\text{OD}_1-\text{H}_1\text{B}$ or OD_2-H_2 , Figure 7), and the second best when all the ligands are deprotonated. In the Cu^{2+} center alone, protonation of Glu-222 (as $\text{OE}_1-\text{H}_1\text{B}$ or OE_2-H_2) produces a geometry with good distance matrix but very poor angles matrix, which, therefore, cannot be considered a good fit to the experimental geometry. In all other cases, protonation of Cys-11, Glu-222, or His-185 produces geometries that are significantly different from the experimental ones. In conclusion, it appears likely that the X-ray structures of the metal centers reflect the existence

in the crystals of a mixed population of ionization states in which either the ligands are fully deprotonated or the sole Asp-233 is protonated as $\text{OD}_1-\text{H}_1\text{B}$ or OD_2-H_2 . As crystals of KDO8PS are maintained at pH = 4.7 (11), it is tempting to speculate that the configuration with Asp-233 protonated (which best reproduces the crystal geometries) is the prevalent form in solution at pH = 5.0 or lower, while the fully deprotonated configuration of the center is the dominant form in solution at pH = 7.0 or higher. With respect to the performance of the three DFT functionals tested, B3LYP gives the best results for the Cd^{2+} and Zn^{2+} centers, while the best results for the Cu^{2+} center are obtained with M06-L and in one case with M06.

Electronic Structure of the Metal Centers in Cd^{2+} and Zn^{2+} KDO8PS. Table 6 shows the distances and angles between the metal and its potential ligands in the Cd^{2+} and Zn^{2+} substituted forms of KDO8PS in complex with PEP, as observed in the X-ray structures and after QM/MM geometry optimization. The wave functions computed at convergence for the QM/MM optimized geometries were employed in a natural bond orbital (NBO) analysis (35), to quantify the contribution of each atom to the electronic structure of the metal center (a listing of the key contributions has been included in the Supporting Information). With regard to this analysis, it is important to recall that a one-center lone pair (LP) NBO n_A is composed of a single normalized natural hybrid orbital (NHO) h_A , while a two-center bond (BD) NBO is a normalized linear combination of two bonding NHOs h_A , h_B , $\Omega_{AB} = a_A h_A + a_B h_B$, with polarization coefficients a_A , a_B satisfying $a_A^2 + a_B^2 = 1$. Depending on the values of these coefficients, a bond NBO ranges between covalent ($a_A = a_B$) and ionic ($a_A \gg a_B$). However, there is no sharp distinction between a highly polar two-center Ω_{AB} ($a_A \gg a_B$) and a one-center n_A ($a_A = 1$, $a_B = 0$). In the NBO analysis, a highly polar Ω_{AB} is identified as a lone pair n_A if 95% or more of the electron density is on a single center ($a_A^2 \geq 0.95$). Accordingly, the occupancy of a Lewis-type LP NBO is typically slightly less than two electrons, indicative of weak delocalization (donation of orbital occupancy) of the electron pair into adjacent non-Lewis acceptor orbitals (particularly, vicinal antibond and Rydberg orbitals).

When all potential metal ligands are deprotonated, the NBO analysis does not identify BD orbitals corresponding to the apparent Lewis structure of the Cd^{2+} center (see Figure 8, and see Supporting Information, Table 1A). The coordination sphere of Cd^{2+} is characterized by a delocalized electronic structure. Second order perturbation theory analysis of the Fock matrix in NBO basis (61) reveals that the strongest contributions to the coordination of Cd^{2+} derive from donation of electron orbital occupancy from valence Lewis-type LP of $\text{SG}^{\text{C}11}$, $\text{NE}2^{\text{H}185}$, $\text{OE}1^{\text{E}222}$, $\text{OD}2^{\text{D}233}$, and O^{WAT} into an unfilled valence non-Lewis-type lone pair (LP*).

Table 5: RMS Deviations between QM/MM and Experimental Geometries^a

	Cd ²⁺ PEP B3LYP	Cd ²⁺ PEP M06	Cd ²⁺ PEP M06-L	Zn ²⁺ PEP B3LYP	Zn ²⁺ PEP M06	Zn ²⁺ PEP M06-L	Cu ²⁺ PEP B3LYP	Cu ²⁺ PEP M06	Cu ²⁺ PEP M06-L	Cu ²⁺ KDO8P B3LYP
all deprotonated	0.216 7.672	0.259 10.628	0.393 17.430	0.257 10.406	0.301 12.483	0.281 10.856	0.496 6.559	0.565 11.538	0.478 6.529	0.266 0.140/11.608
C11-H	0.373 15.943			0.339 13.665			0.597 13.194			
H185-H	0.381 16.895			0.526 17.360			0.543 22.838			
E222-H1	0.495 25.555			0.539 29.191			0.509 22.124			
E222-H1B	1.008 17.713			0.512 22.043			0.493 16.541			
E222-H2	0.499 23.103			0.423 12.416			0.485 20.418			
E222-H2B	0.629 19.695			0.603 18.798			0.739 29.257			
D233-H1	0.234 5.393			0.299 7.390			0.468 8.540			0.295 0.145/11.239
D233-H1B	0.202 6.675	0.261 15.335	0.290 19.318	0.293 9.136	0.319 9.155	0.335 10.119	0.476 8.619	0.441 9.778	0.475 11.631	0.281 0.153/9.859
D233-H2	0.318 13.838			0.448 14.431			0.432 7.581	0.473 8.829	0.388 7.783	0.347 0.252/5.330
D233-H2B	0.256 13.399			0.421 26.780			0.474 8.433			0.298 0.395/7.058
all deprotonated							0.402			
wat_constr							9.020			
D233-H2							0.244	0.259	0.236	
wat_constr							9.273	7.397	6.381	
all deprotonated							0.140			
wat_D233_constr							4.160			

^a Best results are highlighted in bold. For each optimization run, the first number represents the rmsd_{bonds} (in Å), and the second number is the rmsd_{angles} (in degrees). Rms deviations were calculated between the corresponding vectors (one for the X-ray structure and one for the QM/MM optimized structure) composed of the unique elements (21 in total) of the distance matrix relating the metal and all its ligands (Me²⁺, OE1^{E222}, OE2^{E222}, OD1^{E233} or OD2^{E233}, NE2^{H185}, SG^{C11}, and O^{WAT}), and of the angles (15 in total, each one defined by the metal and two ligands) that uniquely describe the geometry of the metal center. Rmsd_{bonds} for the structures containing KDO8P were calculated using a vector composed of 171 unique elements of a distance matrix that contained also the atoms of the product (with only the phosphate moiety excluded). In these cases, italic numbers refer to the rmsd values for the bond and angle vectors that describe just the structure of the metal center. The rows labeled “wat_constr” refer to geometry optimizations carried out constraining the water–Cu²⁺ distance. The row labeled “wat_D233_constr” refers to a geometry optimization carried out constraining both the water–Cu²⁺ and the OD2^{D233}–Cu²⁺ distance. The row labeled “all deprotonated” refers to the geometry optimization carried out with all potential metal ligands deprotonated. The ionization states of KDO8PS explored by QM/MM are defined H1 and H1B for the two positions of a proton on OD1^{D233} or OE1^{E222} and H2 and H2B for the two positions of a proton on OD2^{D233} or OE2^{E222}, as described in Figure 7.

Table 6: Experimental and QM/MM Optimized Geometries of Cd²⁺ and Zn²⁺ Centers in KDO8PS with PEP Bound^a

	Cd ²⁺			Zn ²⁺		
	X-ray	QM/MM		X-ray	QM/MM	
		all ligands deprotonated	D233-H1B		all ligands deprotonated	D233-H1B
SG-M	2.6/2.5	2.7	2.6	2.5/2.5	2.5	2.4
NE2-M	2.4/2.4	2.3	2.4	2.4/2.4	2.1	2.2
OE1-M	2.3/2.3	2.4	2.4	1.9/1.9	2.2	2.2
OE2-M	2.5/2.4	2.7	2.5	2.5/2.4	2.8	2.4
OD2-M	2.0/2.0	2.2	2.4	2.0/1.9	2.1	2.2
O-M	2.5/2.5	2.4	2.4	2.7/3.5	2.4	2.3
SG [^] M [^] NE2	168.2/167.8	169.6	176.7	177.5/151.9	163.7	173.4
SG [^] M [^] OE1	92.4/96.3	92.4	99.1	97.4/101.5	94.9	96.5
SG [^] M [^] OD2	97.4/98.7	109.0	94.2	99.5/98.7	110.8	100.1
OE1 [^] M [^] O	175.9/171.0	170.8	167.2	157.5/174.8	165.7	168.4
OD2 [^] M [^] OE2	143.9/146.7	137.1	144.6	151.0/153.6	138.2	159.7
SG [^] M [^] O	91.0/91.0	89.5	93.3	84.8/82.0	91.0	88.4
NE2 [^] M [^] O	80.1/77.4	90.0	84.1	75.2/70.5	87.2	88.2
OE2 [^] M [^] O	128.3/129.6	119.1	128.4	121.1/123.7	142.1	112.6
OD2 [^] M [^] O	87.7/82.6	99.9	82.1	87.8/82.7	75.9	84.3
geometry		SPY	DO		SPY	DO

^a Optimization carried out with B3LYP. Ligand–metal distances are in Å. Ligand[^]metal[^]ligand angles are in degrees. The two numbers listed in the experimental columns (X-ray) refer to the two active sites present in the asymmetric unit of KDO8PS crystals. Rmsd, root mean square deviation (Å), is between the QM/MM geometry and the experimental one used as the starting point for the optimization. Atom abbreviations: SG, SG^{C11}; OE1, OE1^{E222}; OE2, OE2^{E222}; NE2, NE2^{H185}; OD2, OD2^{D233}; O, O^{WAT}. Abbreviations: M, metal; SPY, square pyramidal; DO, distorted octahedral. The ionization states of KDO8PS explored by QM/MM are defined as in Table 5 and Figure 7.

of the cadmium ion (Figure 8, A–D). The contribution originating from OE2^{E222} is very small; therefore, the geometry of Cd²⁺ in the active site of KDO8PS is essentially

square pyramidal (SPY) with SG^{C11}, NE2^{H185}, OE1^{E222}, and O^{WAT} at the pyramid base and OD2^{D233} at the apex. The natural charge on the Cd ion is +1.6.

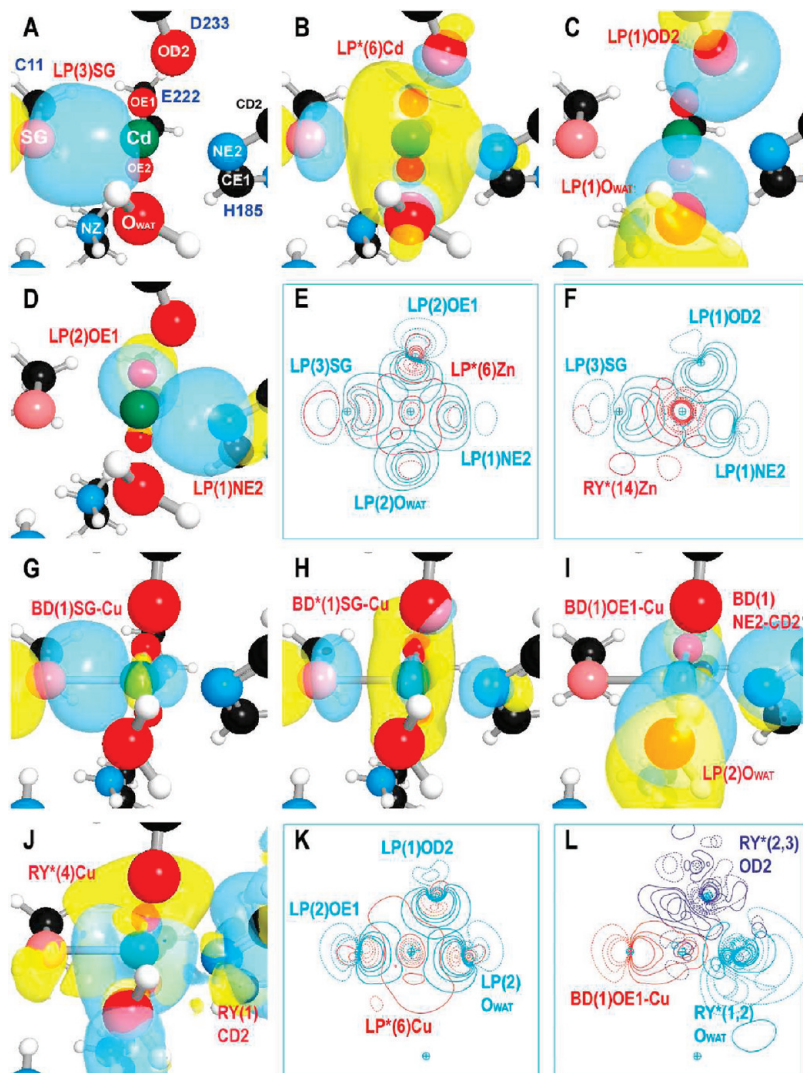


FIGURE 8: Natural localized molecular orbitals (NLMO) in the metal centers of Cd^{2+} , Zn^{2+} , and Cu^{2+} KDO8PS. Panels A–D, 3-D rendering of NLMOs in Cd^{2+} KDO8PS. Panel B, $\text{LP}^{*(6)}\text{Cd}$ accepts orbital occupancy from $\text{LP}^{(3)}\text{SG}^{\text{C}11}$ (panel A), $\text{LP}^{(1)}\text{OD2}^{\text{D}233}$ and $\text{LP}^{(1)}\text{OWAT}$ (panel C), $\text{LP}^{(1)}\text{NE2}^{\text{H}185}$, and $\text{LP}^{(2)}\text{OE1}^{\text{E}222}$ (panel D). Panels E–F, 2-D contours of NLMOs in Zn^{2+} KDO8PS. Panel E, $\text{LP}^{*(6)}\text{Zn}$ (red) accepts orbital occupancy from $\text{LP}^{(3)}\text{SG}^{\text{C}11}$, $\text{LP}^{(2)}\text{OE1}^{\text{E}222}$, $\text{LP}^{(2)}\text{OWAT}$, and $\text{LP}^{(1)}\text{NE2}^{\text{H}185}$ (all in cyan). Panel F, $\text{RY}^{*(14)}\text{Zn}$ (red) accepts orbital occupancy from $\text{LP}^{(3)}\text{SG}^{\text{C}11}$, $\text{LP}^{(1)}\text{OD2}^{\text{D}233}$, and $\text{LP}^{(1)}\text{NE2}^{\text{H}185}$ (all in cyan). Panels G–L, 3-D rendering and 2-D contours of NLMOs in Cu^{2+} KDO8PS. Panel H, $\text{BD}^{*(1)}\text{SG}^{\text{C}11}\text{-Cu}$ accepts orbital occupancy from $\text{BD}^{(1)}\text{SG}^{\text{C}11}\text{-Cu}$ (panel G) and from $\text{BD}^{(1)}\text{OE1}^{\text{E}222}\text{-Cu}$, $\text{BD}^{(1)}\text{NE2-CD2}^{\text{H}185}$, and $\text{LP}^{(2)}\text{OWAT}$ (panel I). Panel J, $\text{RY}^{*(4)}\text{Cu}$ accepts orbital occupancy from the excited $\text{RY}^{(1)}\text{CD2}^{\text{H}185}$. Panel K, $\text{LP}^{*(6)}\text{Cu}$ (red) accepts orbital occupancy from $\text{LP}^{(1)}\text{OD2}^{\text{D}233}$, $\text{LP}^{(2)}\text{OWAT}$, and $\text{LP}^{(2)}\text{OE1}^{\text{E}222}$ (all in cyan). Panel L, $\text{BD}^{(1)}\text{OE1}^{\text{E}222}\text{-Cu}$ donates orbital occupancy to Rydberg orbitals $\text{RY}^{*(2,3)}\text{OD2}^{\text{D}233}$ (blue) and $\text{RY}^{*(1,2)}\text{OWAT}$ (cyan). Abbreviations: BD, bond orbital. LP, lone pair. RY, Rydberg orbital. A * next to the orbital type indicates an unfilled valence or extra valence orbital.

When Asp-233 is protonated as OD1-H1B, the NBO analysis recognizes the presence of a single BD orbital between SG^{C11} and Cd²⁺ (see Supporting Information, Table 1D). This bond is a typical example of the undefined boundaries between covalent bonds and ionic bonds and delocalizations discussed above. In fact, it has a very strong ionic character with 90% of the orbital occupancy associated with a hybrid s^{10%}p^{90%} orbital of SG^{C11} and 10% associated with a hybrid s^{97%}p^{3%} of Cd²⁺. When all the metal ligands are deprotonated (see above) the orbital occupancy on the hybrid orbital of SG^{C11} exceeds 95% and the SG–Cd bond does not qualify as ionic. However, a 3D rendering of the orbitals (not shown) confirms that the two orbitals (LP)SG^{C11} and (LP*)Cd²⁺ of the center with Asp-233 deprotonated are very similar to the two orbitals BD(SG^{C11}–Cd) and BD*(SG^{C11}–Cd) of the metal center with protonated Asp-233. Therefore, in the latter, valence Lewis-type lone pairs (LP) of NE2^{H185},

OE1^{E222}, OD2^{D233}, and OWAT donate occupancy into BD*(SG^{C11}–Cd), rather than into (LP*)Cd²⁺. In the protonated Cd²⁺ center (as OD1–H1B^{D233}), the metal interaction with OE1^{E222} is stronger, and that with NE2^{H185} is weaker than in the unprotonated center (see Supporting Information, Tables 1A and D); thus, if the weak interaction with NE2^{H185} is included, then the geometry of this center can be described as distorted octahedral (DO).

NBO analysis of the Zn²⁺ center shows it to be very similar to the Cd²⁺ center. However, in this case some additional delocalization occurs from the valence Lewis-type LP of SG^{C11}, NE2^{H185}, OE1^{E222}, OD2^{D233}, and OWAT into two unfilled extravalence non-Lewis-type Rydberg orbitals (RY*) of the zinc ion (Figure 8, E,F; see also Supporting Information, Table 1A–C). There is essentially no contribution from OE2^{E222}, and also the geometry of the Zn²⁺ center can be defined as SPY. The natural charge on the Zn ion is +1.6.

Table 7: Experimental and QM/MM Optimized Geometries of the Cu²⁺ Metal Center in KDO8PS with PEP Bound^a

X-ray	QM/MM							
	all deprotonated (B3LYP/M06-L)	D233-H2 (B3LYP/M06-L)	D233-H1B (B3LYP/M06)	all deprotonated Cu(I)	Wat_constr (B3LYP)	D233-H2 (B3LYP/M06-L)	Wat_constr (B3LYP/M06-L)	Wat_D233_constr (B3LYP)
SG-M	2.3/2.3	2.4/2.3	2.3/2.2	2.3/2.3	2.3	2.3	2.3/2.2	2.3
NE2-M	2.1/2.1	2.1/2.1	2.1/2.0	2.1/2.0	2.0	2.1	2.0/2.0	2.0
OE1-M	2.2/2.3	2.1/2.1	2.0/2.1	2.1/2.0	2.5	2.0	2.0/2.0	2.0
OE2-M	2.6/2.6	2.7/2.5	2.7/2.8	2.7/3.0	3.7	2.9	2.8/2.9	2.5
OD2-M	3.0/2.3	2.3/2.0	2.8/3.1	2.6/2.9	3.3	2.0	2.6/2.8	3.0
O-M	2.9/3.2	2.2/2.8	2.1/2.1	2.1/2.0	2.5	3.0	3.0	3.0
SG ⁺ M ⁺ NE2	168.0/165.6	173.6/161.0	172.5/169.3	174.8/171.8	175.2	159.8	167.4/171.4	170.5
SG ⁺ M ⁺ OE1	98.5/97.8	96.2/99.9	93.0/87.9	94.1/91.0	88.8	96.7	96.1/93.6	96.6
SG ⁺ M ⁺ OD2	86.6/93.6	97.6/94.8	89.9/96.9	91.7/86.6	94.8	96.7	84.6/85.3	80.5
OE1 ⁺ M ⁺ O	170.6/173.2	175.7/170.8	172.8/172.8	175.7/175.1	156.6	163.4	160.3/169.2	168.4
OD2 ⁺ M ⁺ OE2	166.4/157.7	162.6/174.3	160.4/158.8	155.0/149.4	154.5	176.0	173.0/163.2	168.4
SG ⁺ M ⁺ O	87.1/87.2	84.7/86.7	87.7/97.8	88.3/91.0	92.3	91.5	83.4/97.1	88.7
NE2 ⁺ M ⁺ O	81.0/78.4	89.9/79.8	91.7/92.5	90.6/93.0	92.5	77.1	86.6/83.7	82.1
OE2 ⁺ M ⁺ O	133.6/130.2	121.2/117.7	119.2/131.4	122.2/127.4	120.8	116.5	108.6/125.8	133.7
OD2 ⁺ M ⁺ O	59.6/69.5	71.1/65.9	78.3/60.5	80.7/77.6	77.8	59.9	68.7/61.6	53.2
geometry	DO	DO	DO	SPL	DT	DT/DTR	DT/ISPY	

^a Symbols and abbreviations are the same as in Tables 5 and 6. Constrained distances are shown in bold. Abbreviations: DO, distorted octahedral; SPL, square planar; DT, distorted tetrahedral; DTR, distorted trigonal; ISPY, incomplete square pyramidal.

When Asp-233 is protonated (as OD1-H1B) the interaction between the metal and OE2^{E222} becomes stronger (see Supporting Information, Table 1D,E), and, thus, the geometry of the center can be described as DO. With regard to the performance of the various DFT functionals in the geometry optimization, NBO analysis of the Zn²⁺ enzyme (for which B3LYP, M06, and M06-L give very similar geometries) shows that the wave functions computed with all three functionals correspond to essentially the same delocalized electronic structure (Supporting Information, Table 1D–F), with M06 and M06-L attributing a stronger ionic character to the SG^{C11}–metal bond than B3LYP.

Electronic Structure of the Metal Center in Cu²⁺ KDO8PS. Table 7 shows the experimental and QM/MM optimized geometries for Cu²⁺ KDO8PS in complex with PEP. The overall best fit to the experimental structure is obtained with M06-L when Asp-233 is protonated as OD2-H2. A slightly inferior result is obtained with B3LYP. However, both functionals reproduce correctly the Cu²⁺–OD2^{D233} distance, but not as well the Cu²⁺–O^{WAT} distance. When all the metal ligands are deprotonated, the best fits are obtained again when the geometry optimization is carried out with B3LYP or M06-L. In this case, B3LYP better reproduces the Cu²⁺–OD2^{D233} distance while M06-L better reproduces the Cu²⁺–O^{WAT} distance. Finally, when Asp-233 is protonated as OD1-H1B M06 gives the best result and reproduces well the Cu²⁺–OD2^{D233} distance, but poorly the Cu²⁺–O^{WAT} distance. NBO analysis of the wave functions corresponding to the three ionization states optimized with B3LYP, M06, or M06-L shows that the open shell (one unpaired 3d electron) electronic structure of the Cu²⁺ center is mostly delocalized like that of Cd²⁺ and Zn²⁺, but also significantly more complex (see Supporting Information, Tables 2A–C and 3A–F). For example, in the structure of the unprotonated center optimized with B3LYP, NBO analysis identifies two BD orbitals with strong ionic character that join SG^{C11} (Figure 8G) and OE1^{E222} (Figure 8 I and L) to Cu²⁺, and donate electron occupancy to each other's corresponding antibonding (BD*) orbitals (one of which is shown in Figure 8H) and to unfilled RY* orbitals of NE2^{H185}, OE1^{E222}, OD2^{D233}, and O^{WAT} (some of which are shown in Figure 8L). Additional strong contributions to the coordination

of Cu²⁺ derive from donation of orbital occupancy from LPs of SG^{C11}, NE2^{H185}, OE1^{E222}, OD2^{D233}, and O^{WAT} into an LP* (Figure 7K) and several RY* orbitals of Cu²⁺ and from LP(2)OWAT and BD(CD2-NE2^{H185}) to BD*(SG^{C11}-Cu) (Figure 8I). Surprisingly, the electronic structure of the copper center also appears to be in an excited state, with a RY orbital of CD2^{H185} (filled at 6% by an excited electron from BD(CD2-NE2^{H185})) donating orbital occupancy to a RY* of copper (Figure 8J). Since the overall contribution from OE2^{E222} to the stability of the Cu²⁺ center is larger than in the other two metals and the vectors connecting OE2^{E222}-Cu and Cu-OD2^{D233} are almost collinear, the geometry of the Cu²⁺ center is best described as DO with OE1^{E222}, OE2^{E222}, OD2^{D233}, and O^{WAT} as the equatorial ligands (pyramid base) and SG^{C11} and NE2^{H185} as the axial ligands. The overall natural charge (alpha + beta spin) on the Cu ion is +1.2. The NBO analysis also reveals that the orbital occupancy donated by LP(3)SG^{Cys11} into one LP* and several RY* orbitals of copper (see Supporting Information, Table 2A) accounts almost entirely for the Cys→Cu²⁺ charge transfer (*16*) that gives origin to an absorption peak at 380 nm in Cu²⁺ substituted KDO8PS (see Experimental Procedures).

As we mentioned, M06-L optimization of the Cu²⁺ center with OD2-H2^{D233} provides the best fit to the experimental geometry (Tables 5, 7). In this case, NBO analysis (see Supporting Information, Table 3C) reveals that the electronic structure is very similar to that of the unprotonated center optimized with B3LYP; two BD orbitals (BD(1)SG–Cu and BD(1)OE1–Cu) with strong ionic character donate electron occupancy to each other's corresponding antibonding (BD*) orbitals and to unfilled RY* orbitals of Cu²⁺, ND1^{H185}, NE2^{H185}, OE1^{E222}, OE2^{E222}, OD2^{D233}, and O^{WAT}. Lone pairs of SG^{C11}, NE2^{H185}, OE1^{E222}, and O^{WAT} also delocalize into LP* and RY* orbitals of Cu²⁺, BD*(SG^{C11}-Cu), and BD*(1)OE1-Cu. The overall natural charge (alpha + beta spin) on the Cu ion is +1.1.

When considering the results obtained with all three DFT functionals, the geometry of the Cu²⁺ center with protonated OD2-H2^{D233} is best described as DO, as that of the fully deprotonated center. The NBO analysis also shows that, although M06-L gives the best geometry, the wave functions

computed with B3LYP, M06, and M06-L correspond to essentially the same delocalized electronic structure (see Supporting Information, Table 3A–C).

Optimization of the Cu^{2+} center with $\text{OD1}-\text{H1B}^{\text{D233}}$ also provides a very good fit to the experimental geometry particularly when the M06 functional is used in the optimization (Tables 5, 7). In this case, the NBO analysis (Supporting Information, Table 3D–F) shows two BD orbitals, $\text{BD}(1)\text{SG}-\text{Cu}$ (more covalent) and $\text{BD}(1)\text{OE1}-\text{Cu}$ (more ionic), and the previously noted network of orbital electron donations from ND1^{H185} , NE2^{H185} , OE1^{E222} , OE2^{E222} , OD2^{D233} , and O^{WAT} into unoccupied valence and extravalence shells of Cu^{2+} . Lone pairs of SG^{C11} , NE2^{H185} , OE1^{E222} , and O^{WAT} also delocalize into LP* and RY* orbitals of Cu^{2+} , $\text{BD}^*(\text{SG}^{\text{C11}}-\text{Cu})$ and $\text{BD}^*(1)\text{OE1}-\text{Cu}$. The overall natural charge (alpha + beta spin) on the Cu ion is +1.03. When considering the results obtained with all three DFT functionals, the geometry of the Cu^{2+} center with $\text{OD1}-\text{H1B}^{\text{D233}}$ is best described as DO, as that of the fully deprotonated center. The NBO analysis also shows that, although M06 gives the best geometry, the wave functions computed with B3LYP, M06, and M06-L correspond to essentially the same delocalized electronic structure.

In another QM/MM simulation (with B3LYP), the copper ion in the quantum region was treated as Cu^+ (Table 7, see also Supporting Information, Table 4) on the assumption that Cu^{2+} might have been reduced to Cu^+ by secondary electrons produced by the X-rays during data collection. In this case, the distance between the metal and OE2^{E222} or OD2^{D233} increased significantly, and NBO analysis of the quantum region showed that these two atoms were no longer involved in the electronic structure of the metal center; as a consequence, the coordination geometry of Cu^+ became SPL with SG^{C11} , OE1^{E222} , NE2^{H185} , and O^{WAT} as ligands. Altogether, while some distances and angles improved slightly with respect to those of the optimized Cu^{2+} center, others worsened, and the rms deviations (0.515 Å for the distance matrix, 11.538° for the angles matrix) of the QM region from the experimental coordinates became larger. Thus, at this point it appears unlikely that Cu^{2+} might have been reduced to Cu^+ during the diffraction experiment.

Constrained QM/MM Simulations of the Metal Center in Cu^{2+} KDO8PS. With regard to the overall geometry of the metal center of Cu^{2+} KDO8PS in complex with PEP, the QM/MM optimization clearly reproduces quite well the Jahn-Teller distortion noted in the X-ray structure (see above), with its uncommon shortening rather than lengthening of the z-axial bonds versus the bonds in the xy plane. However, it is worth noting that, depending on the functional used, either water or OD2^{D233} are much closer (2.2–2.3 Å) to the metal in the QM/MM than in the experimental structure (2.9–3.0 Å) (Table 7). For this reason, some of the calculations were repeated in the presence of a perturbation in the form of a QM dynamic constraint that sets at 3.0 Å the target distance from Cu^{2+} at convergence for either just the water molecule or both O^{WAT} and OD2^{D233} (Tables 5 and 7, columns labeled “wat_{const}” and “wat_D233_{const}”, respectively). By virtue of this perturbation, it was possible to determine the optimal geometry of the Cu^{2+} center, if for molecular reasons that are unknown or cannot be easily incorporated in the model (e.g., long distance geometric or electrostatic effects associated with crystal contacts), water

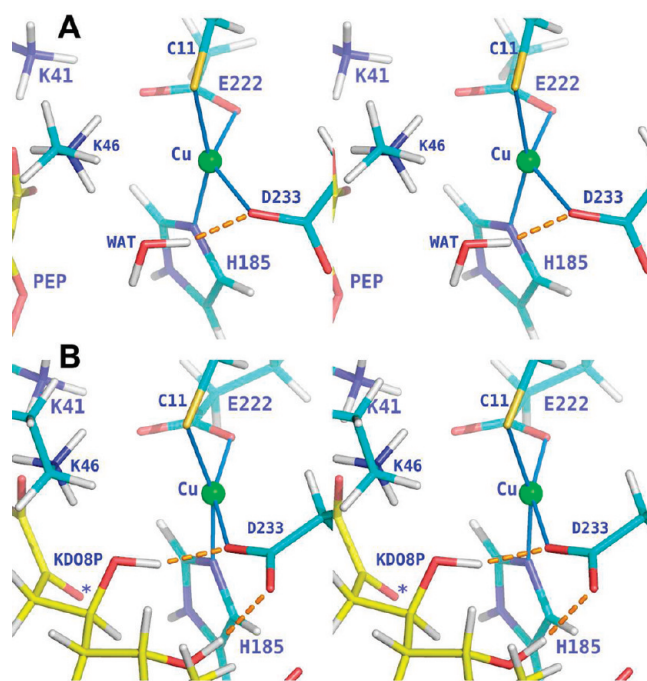


FIGURE 9: Hydrogen bonds of Asp-233 in Cu^{2+} KDO8PS. (A) QM/MM optimized geometry of the active site in Cu^{2+} KDO8PS with bound PEP when a water molecule coordinated to the metal is constrained at a distance of 3.0 Å from it (Table 7). (B) QM/MM optimized geometry of the active site in Cu^{2+} KDO8PS with bound KDO8P. In both panels metal coordination and hydrogen bonds are represented by thin blue lines and dashed orange lines, respectively. In panel B, a star marks the oxygen atom of the product originating from the water molecule originally bound to Cu^{2+} .

and Asp-233 were kept at the distance from the metal observed in the crystal structure.

NBO analysis of the B3LYP optimized quantum region in the QM/MM simulation with all ligands deprotonated and O^{WAT} constrained (see Supporting Information, Table 5) does not show any significant interactions between Cu^{2+} and O^{WAT} and very modest interactions between Cu^{2+} and OE2^{E222} (less than 1/10 the energy of those between Cu^{2+} and OE1^{E222}). Only one BD orbital is present between Cu^{2+} and SG^{C11} . Thus, in this QM/MM optimized structure the metal is coordinated by SG^{C11} , OE1^{E222} , OD2^{D233} , and NE2^{H185} , and the center geometry is distorted tetrahedral (Table 7, see also Figure 9A). The relative positions of O^{WAT} and OD2^{D233} are stabilized by a hydrogen bond between these two atoms (Figure 9A) that originates from donation of orbital occupancy from LPs of OD2^{D233} into the antibonding $\text{BD}^*(\text{O}^{\text{WAT}}-\text{H})$ orbital.

A further improvement of the fit to the experimental coordinates was obtained when, in addition to constraining O^{WAT} at 3.0 Å from Cu^{2+} , protonation of Asp-233 (as $\text{OD2}-\text{H2}^{\text{D233}}$) was also included (Tables 5, 7, see also Supporting Information, Table 6A). In this case, NBO analysis showed that in the B3LYP derived electronic structures there are two BD orbitals with strong ionic character joining Cu^{2+} to SG^{C11} and OE1^{E222} , and a network of orbital donations that coordinate the metal to SG^{C11} , NE2^{H185} , OE1^{E222} , OD2^{D233} and more weakly to OE2^{E222} . There are no significant interactions between Cu^{2+} and O^{WAT} . Thus, if the minor interaction between Cu^{2+} and OE2^{E222} is not considered the geometry of this center, can be described

Table 8: Experimental and QM/MM (B3LYP) Optimized Geometries of the Cu²⁺ Metal Center in KDO8PS with PEP + OH⁻ or KDO8P Bound^a

	+ PEP		+ KDO8P		QM/MM all deprotonated
	X-ray	QM/MM all deprotonated OH ⁻	QM/MM D233-H2 OH ⁻	X-ray	
SG-M	2.3/2.3	2.4	2.4	2.3/2.3	2.4
NE2-M	2.1/2.1	2.1	2.0	2.0/2.1	2.0
OE1-M	2.2/2.3	2.1	2.0	2.2/2.2	2.0
OE2-M	2.6/2.6	3.0	2.7	2.9/2.9	3.1
OD2-M	3.0/2.3	2.3	2.3	2.3/2.6	2.0
O-M	2.9/3.2	2.0	2.2	3.0/3.0	3.2
SG ⁺ M ⁺ NE2	168.0/165.6	171.1	175.0	165.1/162.8	163.4
SG ⁺ M ⁺ OE1	98.5/97.8	90.5	92.5	99.6/100.6	95.4
SG ⁺ M ⁺ OD2	86.6/93.6	100.9	101.2	87.7/86.7	88.7
OE1 ⁺ M ⁺ O	170.6/173.2	162.5	174.2	165.2/165.4	146.6
OD2 ⁺ M ⁺ OE2	166.4/157.7	154.2	142.6	173.9/172.4	155.9
SG ⁺ M ⁺ O	87.1/87.2	90.4	85.3	82.9/80.1	78.1
NE2 ⁺ M ⁺ O	81.0/78.4	92.7	91.6	82.2/82.8	86.4
OE2 ⁺ M ⁺ O	133.6/130.2	113.9	132.5	115.9/116.5	101.2
OD2 ⁺ M ⁺ O	59.6/69.5	88.7	82.2	64.9/59.2	55.3
geometry		DO	DO		DT

^a Symbols and abbreviations are the same as in Tables 6 and 7 with the exception that O stands for O^{WAT} in the enzyme complex with PEP and for C4-OH^{KDO8P} in the enzyme complex with KDO8P. Abbreviations: DO, distorted octahedral; DT, distorted tetrahedral.

as distorted tetrahedral (Table 7). In the M06-L derived electronic structure (see Supporting Information, Table 6B), there is one BD orbital with covalent character joining SG^{C11} to Cu²⁺, and several donations of orbital occupancy that coordinate the metal to SG^{C11}, NE2^{H185}, and OE1^{E222}. There are no significant interactions between Cu²⁺ and OE2^{E222}, OD2^{D233}, or O^{WAT}. With the noted difference that only one of the carboxylate oxygens of Glu-222 interacts with the Cu²⁺ ion, this geometry is very similar to that described below for the structure in which both O^{WAT} and OD2^{D233} were constrained (Table 7) and can be defined as distorted trigonal (DTR) or incomplete trigonal pyramidal (ITPY).

Finally, the overall best fit of the QM/MM optimized structure to the experimental structure was obtained when both O^{WAT} and OD2^{D233} were constrained (row labeled all deprotonated wat_D233_constr in Tables 5, 7). NBO analysis of the quantum region (see Supporting Information, Table 7) shows some of the interactions already noted for the unconstrained simulation (e.g., bonding orbitals between Cu²⁺ and SG^{C11} and between Cu²⁺ and OE1^{E222}) and some new strong interactions between Cu²⁺ and OE2^{E222} (as donation of orbital occupancy from BD(1)SG-Cu and BD(1)OE1-Cu into RY* orbitals of OE2^{E222}). No significant interactions are present between Cu²⁺ and O^{WAT} or OD2^{D233}, which, therefore, cannot be considered as metal ligands. Thus, in this QM/MM optimized geometry, which best resembles the experimental structure of the Cu²⁺ enzyme with bound PEP, the metal is coordinated solely by the thiolate of Cys-11, by both of the carboxylate oxygens of Glu-222, and by the unprotonated nitrogen of His-185. We have found only one report of a similar Cu²⁺ geometry in the MESPEUS database (62) of metal centers in proteins, as seen in the structure of the double mutant M37L/P40S of *E. coli* thioredoxin (PDB entry 1KEB); in that case, the geometry was listed as distorted tetrahedral or square pyramidal with one ligand missing. Accordingly, we are classifying the geometry of the Cu²⁺ center in the QM/MM optimized structure as distorted tetrahedral/incomplete square pyramidal (DT/ISPY); either the O^{WAT} or the OD2^{D233} can be considered as the missing ligand. Also in this structure,

the relative positions of O^{WAT} and OD2^{D233} are stabilized by a donation of orbital occupancy from LPs of OD2^{D233} into the antibonding BD*(O^{WAT}-H) orbital.

QM/MM Simulations of a Hydroxide Ion as a Metal Ligand in KDO8PS. It has been postulated that one function of the metal in KDO8PS might be to favor deprotonation of the coordinated water (11). However, when the geometry of the active site is optimized by QM/MM in the presence of a hydroxide ion in place of water, the hydroxide ion extracts a proton from the nearby Lys-46, and the minimization converges to a geometry that is essentially identical to that observed when water is present from the start (Table 8, Figure 10). Proton transfer from Lys-46 to the hydroxide ion was observed also when the simulation was carried out with the Zn²⁺ enzyme and with or without inclusion of PEP in the QM region (not shown), suggesting that this event is not a unique feature of the Cu²⁺ center. However, if the simulation is carried out in the presence of protonated Asp-233 (as OD2-H2), then the hydroxide ion preferentially extracts a proton from Asp-233 rather than from Lys-46. Also in this case, the geometry finally converged to that of the unprotonated center with water bound to the metal (Table 8).

QM/MM Simulations of KDO8PS Active Site with Product Bound. In a different set of experiments the geometry of the Cu²⁺ center in the enzyme with bound KDO8P and Pi was also optimized by QM/MM using B3LYP as the DFT functional (Tables 5, 8). In addition to both products, Lys-124 and Arg-154 were included in the quantum region, as they neutralize the negative charge on the free phosphate. It is of mechanistic relevance to ascertain whether Asp-233 is protonated at the end of the reaction of KDO8P synthesis (see Discussion). For this reason, the geometry optimization of the product bound active site was carried out in all possible ionization states of Asp-233 (as shown in Figure 7). The best fit to the experimental structure was obtained with Asp-233 deprotonated. NBO analysis of the quantum region (see Supporting Information, Table 8) indicates that the coordination and geometry of Cu²⁺ are very similar to those observed in the QM/MM optimized structure of the enzyme in complex with PEP when only O^{WAT} is constrained at 3.0 Å

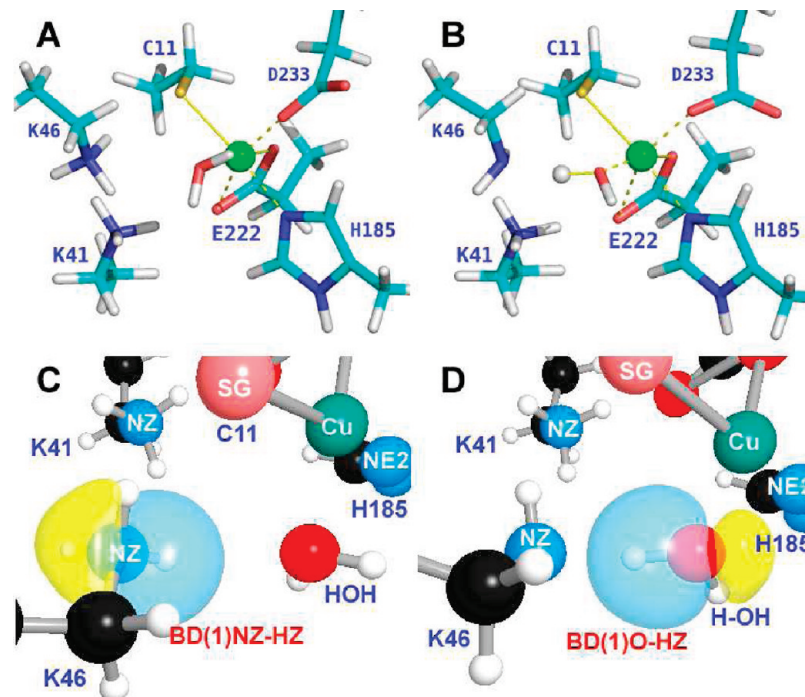


FIGURE 10: Proton transfer from Lys-46 to a hydroxide ion in Cu^{2+} KDO8PS. (A) QM/MM optimized geometry of the active site in Cu^{2+} KDO8PS when a water molecule is coordinated to the metal. (B) QM/MM optimized geometry of the active site in Cu^{2+} KDO8PS when a hydroxide ion is coordinated to the metal. (C) Same as panel A, but showing the BD between NZ^{46} and HZ1^{46} . (D) Same as panel B, but showing that the BD orbital between NZ^{46} and HZ1^{46} is replaced by a BD orbital between O^{OH} and HZ1^{46} , at the same time as Lys-46 becomes neutral.

from the metal. Thus, when KDO8P is bound in the active site, it does not interact with Cu^{2+} (which is coordinated solely by $\text{SG}^{\text{C}11}$, $\text{OE1}^{\text{E}222}$, $\text{OD2}^{\text{D}233}$, and $\text{NE2}^{\text{H}185}$), and the geometry of the metal center is distorted tetrahedral (Table 8, Figure 9B). The relative positions of the product and the carboxylate of Asp-233 are stabilized by hydrogen bonds between $\text{C4-OH}^{\text{KDO8P}}$ and $-\text{OD2}^{\text{D}233}$ and between $\text{C6-OH}^{\text{KDO8P}}$ and $-\text{OD1}^{\text{D}233}$ (Figure 9B). NBO analysis of the QM region shows that these bonds are, in fact, due to donation of orbital occupancy from LPs of the carboxylate oxygens of Asp-233 into LP*^s and RY*^s orbitals of the hydroxyl hydrogens of KDO8P and into the antibonding BD*(O-H) orbitals of these hydroxyl groups.

Electronic Structure of the Cd^{2+} , Zn^{2+} , and Cu^{2+} Metal Centers in the Gas Phase. It is important to know whether the QM/MM optimized geometry of the metal centers is determined solely by the chemical nature of the ligands or also by the protein environment (dielectric constant, hydrophobic and electrostatic interactions). The idealized geometries that the metal centers would acquire, if the same ligands were not immersed in the protein environment, were derived by building simplified model metal centers that mirrored the active sites of metal-substituted KDO8PS. Cys-11, His-185, Glu-222, Asp-233, and the metal-proximal water were extracted from the crystal structures of the KDO8PS·PEP complexes. Cys-11 was converted to ethylthiolate, His-185 to imidazole, and Glu-222 and Asp-233 to acetate. Spin unrestricted, full QM geometry optimizations of the model metal centers were carried out in the gas phase with the B3LYP DFT functional using the same level of theory as described for the QM component of the QM/MM runs inside the protein environment. In all three metal forms of KDO8PS, during the early stage of geometry optimization,

Table 9: QM Gas-Phase Optimized Geometries of KDO8PS Model Metal Centers^a

	Cd^{2+}	Zn^{2+}	Cu^{2+}
C11SG-M	2.5	2.4	2.3
H185NE2-M	2.4	2.2	2.1
E222OE1-M	2.3	2.0	2.0
E222OE2-M	3.7	3.3	3.5
D233OD2-M	2.2	2.0	2.0
$\text{C11SG}^{\text{M}}\text{H185NE2}$	115.4	116.7	146.0
$\text{C11SG}^{\text{M}}\text{E222OE1}$	111.4	114.9	98.8
$\text{C11SG}^{\text{M}}\text{D233OD2}$	124.2	116.4	95.6
$\text{D233OD2}^{\text{M}}\text{E222OE1}$	100.3	112.6	148.5
geometry	T	T	DT

^a Ligands–metal distances are in Å. Ligand^ametal^bligand angles are in degrees. Abbreviations: T, tetrahedral; DT, distorted tetrahedral.

water was squeezed out of the metal coordination sphere, which, therefore, included only model compounds for Cys-11, His-185, Glu-222, and Asp-233. At convergence, the gas-phase optimized geometry was tetrahedral (Cd^{2+} and Zn^{2+}) or distorted tetrahedral (Cu^{2+}) (Table 9, Figure 11). Similar geometries were obtained when the optimization was performed under conditions of solvation in water (not shown), suggesting that the differences between the model metal centers and the protein metal centers are not due to the enhancement of electrostatic interactions occurring in vacuo between the ligands. However, this observation does not rule out that such differences may be due to hydrophobic and electrostatic interactions of the ligands themselves with the rest of the protein (see below). Finally, it is worth noting that also in the gas phase the QM optimization captures well the nature of the Jahn–Teller distortion of the Cu^{2+} complex. In this case, the instability of the tetrahedral Cu(II) complex is lifted by a D_{2d} distortion toward a tetragonal geometry.

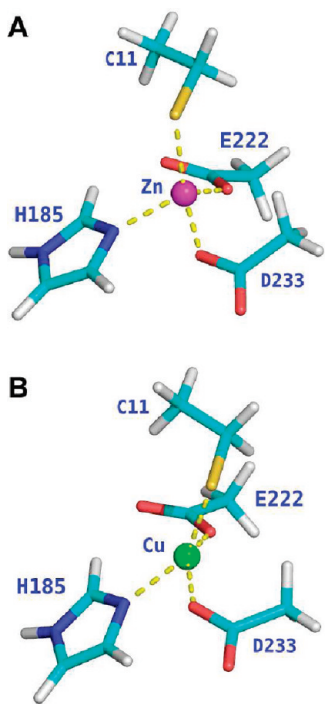


FIGURE 11: QM gas-phase optimized geometry of KDO8PS model metal centers. (A) Zn^{2+} center: the geometry is almost perfectly tetrahedral. (B) Cu^{2+} center: the geometry is distorted (flattened) tetrahedral. Labels refer to the corresponding residues in the protein environment.

DISCUSSION

A remarkable feature of KDO8PS is that two almost identical forms of this enzyme exist, with and without metal in the active site (15, 16). Several divalent cations have been reported to provide various levels of activity (16, 19) to the metal form, but no correlation has been presented between the level of activity with different metals and the structural and electronic characteristics of the metal centers. In this work, we have studied in detail the Cd^{2+} , Zn^{2+} , and Cu^{2+} substituted forms of KDO8PS. When only the k_{cat} and K_m kinetic constants are considered, the three metal-substituted forms derived from the same enzyme preparation (Prep 1, Table 2) show similar behavior under a wide range of conditions (Figure 2) with Zn^{2+} providing the highest activity and Cu^{2+} the lowest. However, it is worth noting that inevitably there is some difference in activity from prep to prep, and, for example, a second independent preparation of the Cd^{2+} enzyme (Prep 2, Table 2) displayed a higher activity than the Zn^{2+} enzyme, in line with earlier observations (16). At low A5P concentrations ($1\text{--}10 \mu M$), flux control in the Zn^{2+} enzyme deviates significantly from that of the other two metals, as the control exerted by the condensation reaction (Figure 3, Step R3) is much smaller in comparison, and that exerted by the binding of A5P (Figure 3, Step R2) is much larger.

In the crystal environment, the Cu^{2+} enzyme is the only form that shows some level of activity, as for the first time KDO8P in its linear form is observed bound in the active site (Figures 5, 6), a result probably aided by the fact that the flux control by the product release step appears to be particularly relevant in Cu^{2+} KDO8PS (Figure 3, Step R4). The positions of the chemical moieties of KDO8P with respect to the side chains that make up the active site cavity

are very similar to those observed in the reaction intermediate INT visualized in the structure of the metal-free C11N/S235P/Q237A mutant KDO8PS (compare Figure 6 of this study to Figure 5 in 13). This observation suggests that the reaction mechanism must be essentially identical in both metal and nonmetal KDO8PS. It is also important to notice that the $C4-OH^{KDO8P}$ occupies essentially the same position and shows the same pattern of hydrogen bonding to $OD2^{D233}$ as water does in the constrained QM/MM optimization of the Cu^{2+} enzyme with PEP bound (Figure 9). For this reason, one can easily argue that this must also be the position that the carbonyl oxygen of A5P ($O1^{A5P}$, which will become $C4-OH^{KDO8P}$) occupies at some point during the condensation reaction.

In previous work we have reported that in different structures A5P appears in one of two possible conformations. In one conformation, the water bound to the metal (or hydrogen bonded to Asn-11 in the metal-free C11N mutant) is replaced by $C2-OH^{A5P}$ (conformation A). This is the conformation of A5P observed also in the structure of Zn^{2+} -KDO8PS in complex with PEP and A5P (Figure 5B). A variation of this conformation, in which water is retained and A5P is shifted, is observed in the structure of the Cd^{2+} enzyme (Figure 5A, see also 11). In these conformations, A5P is rotated by 180° around its long axis with respect to the positions that its atoms assume in INT or KDO8P. For this reason, conformation A is not expected to be catalytically competent, and we have not pursued its investigation by a QM/MM approach. In the other conformation (conformation B), water is replaced by the aldehyde carbonyl of A5P ($O1^{A5P}$) (see Figure 4D in 13). Since this water is believed to be involved in attacking the *si* side of $C2^{PEP}$ in order to form INT with the correct chirality at the C2 center (13), conformation B is also catalytically inactive. However, it may be similar to the catalytically competent conformation of A5P, as all the hydroxyl groups of A5P are in the same positions they assume in INT (in metal-free KDO8PS (13)) and in KDO8P (in Cu^{2+} KDO8PS, this study). On this basis, we propose that the reaction does not start when A5P reaches the position observed in the X-ray structures (which would be a dead end), but at some earlier point along its path into the active site. It is conceivable that as the aldehyde moiety of A5P approaches the metal bound water, the water deprotonates, and the resulting hydroxide ion attacks $C2^{PEP}$. In the next stage of catalysis, a transient tetrahedral $C2$ -hydroxylated derivative of PEP would react with $C1^{A5P}$, while $O1^{A5P}$ picks up a proton (perhaps from the previous acceptor) becoming $C4-OH^{INT}$ (Figure 1).

The carboxylate oxygen ($OD2$) of Asp-233 is the closest potential acceptor of a proton from water in order to generate the hydroxide ion and would be well positioned to return the proton to the product (Figures 6, 9, see also NBO analysis of the unprotonated Cu^{2+} center with KDO8P bound, above). However, it is important to remember that the electronic configuration of the active site is in a noncatalytic state when only PEP is bound (to prevent its wasteful breakdown as a consequence of a hydroxide attack not followed by a condensation step), but must be able to shift rapidly to a catalytic state when A5P comes in. In the constrained QM/MM optimized structure of the Cu^{2+} center with PEP bound (Table 7, column labeled “wat_constr”), the observed donation of orbital occupancy from LPs of $OD2^{D233}$ into the antibonding

$\text{BD}^*(\text{O}^{\text{WAT}}-\text{H})$ orbital is similar to the donation of orbital occupancy from LPs of OD2^{D233} into LP*s and RY*s orbitals and into the antibonding $\text{BD}^*(\text{O}-\text{H})$ orbitals of the hydroxyl hydrogen of C4-OHKDO8P (Figure 9). However, this donation is not sufficient to produce a proton capture by the carboxylate oxygen of Asp-233. In fact, the QM/MM optimization of a hydroxide ion in the Cu^{2+} metal center with Asp-233 protonated as OD2-H2 (Table 8) shows that the hydroxide ion would capture a proton from Asp-233 rather than the other way around. Likewise, the QM/MM optimization of a hydroxide ion in the Zn^{2+} or Cu^{2+} metal center with PEP bound shows that even if water deprotonation occurred in the presence of just PEP and without proton transfer to Asp-233, the resulting hydroxide ion would be unstable and would rapidly capture a proton from the nearby Lys-46 (Figure 10), bringing the reaction to a halt.

Thus, the electronic structure of the metal center in the resting enzyme is tailored to prevent a generation of a hydroxide ion from water and its potentially wasteful reaction with PEP. However, during the early stage of the condensation reaction the incoming O1^{A5P} might somehow favor a temporary proton capture by OD2^{D233} and the generation of a hydroxide ion that might be more stable in the new electronic environment generated by the presence of A5P. At the end of the condensation reaction, O1^{A5P} would be already positioned to recapture a proton from OD2^{D233} .

Altogether, the kinetic, crystallographic, and computational data gathered in this study only partially support this proton shuttle mechanism. In fact, regardless of the metal studied, the QM/MM simulation suggests that the X-ray structures can be interpreted as representing a metal center in which Asp-233 is at least partially protonated (Table 5), most likely as a consequence of the fact that crystals of KDO8P synthase are only stable in the pH = 4.5–5.5 range. If transfer of a proton from water to Asp-233 was necessary for catalysis, then we might expect the reaction to proceed much more slowly at pH = 5.0 versus pH = 7.5. Instead, for both the Cd^{2+} and Cu^{2+} enzyme, while K_m^{PEP} , K_m^{A5P} , K_d^{KDO8P} , $K_d^{\text{P}_i-1}$, and $K_d^{\text{P}_i-2}$ are affected to various extents at pH = 5.0, k_{cat} remains essentially unchanged from pH = 7.5 (Table 2). On the other hand, QM/MM simulations of the active site with both KDO8P and P_i bound in different ionization states of Asp-233 (Table 5) slightly favor an interpretation of the X-ray structure as representing a metal center in which Asp-233 is deprotonated at the end of the reaction. Thus, it is indeed possible that the ionization state of Asp-233 is modulated by A5P; in the absence of this substrate, Asp-233 would be protonated and prevent water activation, while in the presence of A5P, Asp-233 would be deprotonated and favor hydroxide generation.

The QM/MM optimization of the Cd^{2+} , Zn^{2+} , and Cu^{2+} ligand fields has identified some important characteristics of these centers. The most remarkable finding is that the electronic structure of the centers is mostly delocalized (Figure 8; see Supporting Information). This observation was confirmed by carrying out the geometry optimizations with three different DFT functionals (B3LYP, M06, and M06-L) (Table 5). B3LYP provided the most accurate representation of the Cd^{2+} and Zn^{2+} centers, but in most cases M06-L gave the best representation of the Cu^{2+} center (although with 2–3 times longer convergence times with respect to B3LYP). While the optimized geometries obtained with the three functionals are slightly different from each other, NBO analysis of the corresponding wave functions

revealed that they all converge to essentially the same electronic structures. In the NBO formalism adopted in this study, a highly polar Ω_{AB} was identified as a covalent bond (BD) if the electron density is distributed equally between the two centers, and as an ionic BD if the electron density on one of the two centers is $\gg 50\%$ and $< 95\%$ (see above). Based on this definition, the only bona fide ligand–metal bonding orbitals (each with significant ionic character) involve the thiolate sulfur of Cys-11 and a carboxylate oxygen of Glu-222 (this latter only in the Cu^{2+} enzyme). All other ligand–metal interactions are based on a modest donation of orbital occupancy ($\ll 5\%$) from ligand lone pairs into unfilled valence or extravalence orbitals of the metal (see Supporting Information). The absence of a defined Lewis structure is responsible for some plasticity in the type of geometry that can be observed in different active sites of the same tetrameric enzyme. For example, in the second active site of Zn^{2+} KDO8PS, water (at 3.5 Å from Zn^{2+}) is out of the coordination sphere of the zinc ion and the geometry of the metal center (distorted tetrahedral) resembles more closely that obtained by QM gas-phase optimization (Figure 11), than that derived by QM/MM optimization in the protein environment. The Cu^{2+} enzyme also displays a variable metal geometry ranging from an octahedral center, in which water is bound to the metal, to a heavily distorted tetrahedral center, in which neither water nor KDO8P is bound to the metal.

The second critical observation is that the experimental (X-ray) geometries are similar to the QM/MM optimized geometries, but very different from the geometries optimized in QM gas phase (with the exception noted above). This fact indicates that the 3-D fold of KDO8PS has evolved not just to place ligands at the positions in space required by the ideal geometry of the metal (with those ligands), but rather to create a specific geometry and electronic structure that best meets the catalytic requirements. A difference between the geometry of a metal center in model compounds and that observed inside a protein has often been attributed to an entatic effect (from the Greek *εντασις*, or strain) exerted by the protein on the metal center. This concept of an entatic or energized state for metallo-proteins and enzymes in general was first introduced to explain the unusual spectral (visible and EPR) and redox properties of blue-copper proteins, ferredoxins, and some cytochromes (63, 64). In particular, in blue-copper proteins the strained metal center geometry imposed by a stiff protein has been associated with the need to lower the reorganization energy associated with the change in redox state, in order to achieve fast electron transfer rates (65). However, the concept of entasis was not well defined in these studies; it appeared to be close to Warshel's rigorous definition of strain as a mechanical distortion due to covalent interactions (66), in which case it is doubtful whether it could contribute significantly to enzyme catalysis in general (66–68). Instead, it is important to consider that any metal center acquires different properties when bound to a protein due to the fact that the protein environment has different dielectric constant from vacuum or solution, and that it provides highly specific hydrophobic and electrostatic interactions dependent on the unique fold and charge distribution of each protein. On this basis, it may be more correct to view the geometry of the metal center observed in KDO8PS not as an energized state due to the strain exerted by the protein but, quite the opposite, as reflective of the fact that the energy minimum of the center is very different in the protein versus the gas-phase, and that the protein has evolved to achieve this different energy minimum,

presumably to improve catalysis. This view is supported by QM simulations of the metal centers of blue-copper proteins (whose investigation prompted the original proposal of an entatic state), which clearly show that there is no strain in these centers (69), and that the small reorganization energies associated with different redox states are due to an appropriate choice of metal ligands, and in particular to the presence of a flexible metal–methionine bond that can change geometry at virtually no cost (70). This mechanism is actually the antithesis of the strain hypothesis, which relies instead on rigid bonds. KDO8PS does not carry out redox cycling, but part of the energy cost of the condensation reaction is likely to originate from the reorganization energy of the metal center between the substrate-bound and product-bound states. Thus, the different shape (and the associated energy minimum) of the metal center in the active site of KDO8PS versus in vacuo may be the result of an evolutionary process aimed at achieving a relatively flat potential energy surface between the metal geometries that exist at different stages of catalysis.

ACKNOWLEDGMENT

We thank Dr. Sharon Ackerman for her critical evaluation of the manuscript.

SUPPORTING INFORMATION AVAILABLE

Key interactions in the metal center of Cd²⁺, Zn²⁺, and Cu²⁺ KDO8PS as determined by NBO analysis. Coordinates used for the NBO analysis of the Cd²⁺ metal center with PEP bound. Coordinates used for the NBO analysis of the Zn²⁺ metal center with PEP bound. Coordinates used for the NBO analysis of the Cu²⁺ metal center with PEP bound. Coordinates used for the NBO analysis of the Cu²⁺ metal center with PEP bound and O^{WAT} constrained. Coordinates used for the NBO analysis of the Cu²⁺ metal center with PEP bound and O^{WAT} and OD2D²³³ constrained. Coordinates used for the NBO analysis of the Cu²⁺ metal center with KDO8P bound. This material is available free of charge via the Internet at <http://pubs.acs.org>.

REFERENCES

1. Raetz, C. R. (1990) Biochemistry of endotoxins. *Annu. Rev. Biochem.* **59**, 129–170.
2. Ray, P. H., Kelsey, J. E., Bigham, E. C., Benedict, C. D., and Miller, T. (1983) Synthesis and use of 3-deoxy-D-manno-2-octulosonate (KDO) in *Escherichia coli*: Potential sites of inhibition, in *ACS Symposium Series* (Anderson, L., Unger, F. M., Eds.), pp 141–169, American Chemical Society, Washington, D.C.
3. Levin, D. H., and Racker, E. (1959) Condensation of arabinose 5-phosphate and phosphorylenol pyruvate by 2-keto-3-deoxy-phosphoctic acid synthetase. *J. Biol. Chem.* **234**, 2532–2539.
4. Rick, P. D., and Young, D. A. (1982) Isolation and characterization of a temperature-sensitive lethal mutant of *Salmonella typhimurium* that is conditionally defective in 3-deoxy-D-manno-octulosonate-8-phosphate synthesis. *J. Bacteriol.* **150**, 447–455.
5. Rick, P. D., Neumeyer, B. A., and Young, D. A. (1984) Effect of altered lipid: A synthesis on the synthesis of major proteins of the *Salmonella typhimurium* outer membrane. *Rev. Infect. Dis.* **6**, 455–462.
6. Kohen, A., Jakob, A., and Baasov, T. (1992) Mechanistic studies of 3-deoxy-D-manno-2-octulosonate-8-phosphate synthase from *Escherichia coli*. *Eur. J. Biochem.* **208**, 443–449.
7. Kohen, A., Berkovich, R., Belakhov, V., and Baasov, T. (1993) Stereochemistry of KDO8P synthase. An efficient synthesis of the 3-fluoro analogs of KDO8P. *Bioorg. Med. Chem. Lett.* **3**, 1577–1582.
8. Dotson, G. D., Nanjappan, P., Reily, M. D., and Woodard, R. W. (1993) Stereochemistry of 3-deoxyoctulosonate 8-phosphate synthase. *Biochemistry* **32**, 12392–12397.
9. Dotson, G. D., Dua, R. K., Clemens, J. C., Wooten, E. W., and Woodard, R. W. (1995) Overproduction and one-step purification of *Escherichia coli* 3-deoxy-D-manno-octulosonic acid 8-phosphate synthase and oxygen transfer studies during catalysis using isotopic-shifted heteronuclear NMR. *J. Biol. Chem.* **270**, 13698–13705.
10. Li, Z., Sau, A. K., Shen, S., Whitehouse, C., Baasov, T., and Anderson, K. S. (2003) A snapshot of enzyme catalysis using electrospray ionization mass spectrometry. *J. Am. Chem. Soc.* **125**, 9938–9939.
11. Duewel, H. S., Radaev, S., Wang, J., Woodard, R. W., and Gatti, D. L. (2001) Substrate and metal complexes of 3-deoxy-D-manno-octulosonate 8-phosphate synthase from *Aquifex aeolicus* at 1.9 Å resolution: implications for the condensation mechanism. *J. Biol. Chem.* **276**, 8393–8402.
12. Wang, J., Duewel, H. S., Woodard, R. W., and Gatti, D. L. (2001) Structures of *Aquifex aeolicus* KDO8P synthase in complex with R5P and PEP and with a bisubstrate inhibitor: role of active site water in catalysis. *Biochemistry* **40**, 15676–15683.
13. Kona, F., Xu, X., Martin, P., Kuzmic, P., and Gatti, D. L. (2007) Structural and mechanistic changes along an engineered path from metallo- to nonmetallic 3-deoxy-D-manno-octulosonate 8-phosphate synthases. *Biochemistry* **46**, 4532–4544.
14. Hedstrom, L., and Abeles, R. (1988) 3-Deoxy-D-manno-octulosonate-8-phosphate synthase catalyzes the C–O bond cleavage of phosphoenolpyruvate. *Biochem. Biophys. Res. Commun.* **157**, 816–820.
15. Birck, M. R., and Woodard, R. W. (2001) *Aquifex aeolicus* 3-deoxy-D-manno-2-octulosonic acid 8-phosphate synthase: a new class of KDO 8-P synthase? *J. Mol. Evol.* **52**, 205–214.
16. Duewel, H. S., and Woodard, R. W. (2000) A metal bridge between two enzyme families. 3-deoxy-D-manno-octulosonate 8-phosphate synthase from *Aquifex aeolicus* requires a divalent metal for activity. *J. Biol. Chem.* **275**, 22824–22831.
17. Wang, J., Duewel, H. S., Stuckey, J. A., Woodard, R. W., and Gatti, D. L. (2002) Function of His-185 in *Aquifex aeolicus* 3-deoxy-D-manno-octulosonate 8-phosphate synthase. *J. Mol. Biol.* **324**, 205–214.
18. Xu, X., Kona, F., Wang, J., Lu, J., Stemmler, T., and Gatti, D. L. (2005) The catalytic and conformational cycle of *Aquifex aeolicus* KDO8P synthase: role of the L7 loop. *Biochemistry* **44**, 12434–12444.
19. Shulami, S., Furdui, C., Adir, N., Shoham, Y., Anderson, K. S., and Baasov, T. (2004) A reciprocal single mutation affects the metal requirement of 3-deoxy-D-manno-2-octulosonate-8-phosphate (KDO8P) synthases from *Aquifex pyrophilus* and *Escherichia coli*. *J. Biol. Chem.* **279**, 45110–45120.
20. Duggleby, R. G. (1995) Analysis of enzyme progress curves by nonlinear regression. *Methods Enzymol.* **249**, 61–90.
21. Beechem, J. M. (1992) Global analysis of biochemical and biophysical data. *Methods Enzymol.* **210**, 37–54.
22. Kuzmic, P. (1996) Program DYNAFIT for the analysis of enzyme kinetic data: application to HIV proteinase. *Anal. Biochem.* **237**, 260–273.
23. Hoops, S., Sahle, S., Gauges, R., Lee, C., Pahle, J., Simus, N., Singhal, M., Xu, L., Mendes, P., and Kummer, U. (2006) COPASI—a Complex PAthway SImulator. *Bioinformatics* **22**, 3067–3074.
24. Duewel, H. S., Sheflyan, G. Y., and Woodard, R. W. (1999) Functional and biochemical characterization of a recombinant 3-deoxy-D-manno-octulosonic acid 8-phosphate synthase from the hyperthermophilic bacterium *Aquifex aeolicus*. *Biochem. Biophys. Res. Commun.* **263**, 346–351.
25. Otwinowski, Z., and Minor, W. (1997) Processing of X-ray diffraction data collected in oscillation mode. *Methods Enzymol.* **276**, 307–326.
26. Engh, R. A., and Huber, R. (1991) Accurate bond and angle parameters for X-ray protein structure refinement. *Acta Cryst. Allogr.* **A47**, 392–400.
27. Adams, P. D., Pannu, N. S., Read, R. J., and Brunger, A. T. (1997) Cross-validated maximum likelihood enhances crystallographic simulated annealing refinement. *Proc. Natl. Acad. Sci. U.S.A.* **94**, 5018–5023.
28. Warshel, A., and Levitt, M. (1976) Theoretical studies of enzymic reactions: dielectric, electrostatic and steric stabilization of the carbonium ion in the reaction of lysozyme. *J. Mol. Biol.* **103**, 227–249.
29. Lee, F. S., Chu, Z. T., and Warshel, A. (1993) Microscopic and semimicroscopic calculations of electrostatic energies in proteins

- by the POLARIS and ENZYMIK Programs, *J. Comput. Chem.* 14, 161–185.
30. Becke, A. D. (1993) Density-functional thermochemistry III. The role of exact exchange. *J. Chem. Phys.* 98, 5648–5652.
 31. Stephens, P. J., Devlin, F. J., Chabalowski, C. F., and Frisch, M. J. (1994) Ab initio calculation of vibrational absorption and circular dichroism spectra using density functional force fields. *J. Phys. Chem.* 98, 11623–11627.
 32. Zhao, Y., and Truhlar, D. G. (2006) A new local density functional for main-group thermochemistry, transition metal bonding, thermochemical kinetics, and noncovalent interactions. *J. Chem. Phys.* 125, 194101–194118.
 33. Jorgensen, W. L., and Tirado-Rives, J. (1988) The OPLS force field for proteins. Energy minimizations for crystals of cyclic peptides and crambin. *J. Am. Chem. Soc.* 110, 1657–1666.
 34. Dean, M., and Philipp, R. A. F. (1999) Mixed $\text{Q}\text{M}/\text{M}\text{M}$ modeling using frozen orbitals and tests with alanine dipeptide and tetrapeptide. *J. Comput. Chem.* 20, 1468–1494.
 35. Weinhold, F. (1998) Natural Bond Orbital Methods, in *Encyclopedia of Computational Chemistry* (von Ragué Schleyer, P., Schreiner, P. R., Allinger, N. L., Clark, T., Gasteiger, J., Kollman, P. A., Schaefer III, H. F., Ed.), pp 1792–1811, John Wiley & Sons, Chichester, UK.
 36. Field, M. J., Bash, P. A., and Karplus, M. (1990) A combined quantum mechanical and molecular mechanical potential for molecular dynamics simulations. *J. Comput. Chem.* 11, 700–733.
 37. King, E. L., and Altman, C. (1956) A schematic method of deriving the rate laws for enzyme-catalyzed reactions. *J. Phys. Chem.* 60, 1375–1378.
 38. Segel, I. (1975) *Enzyme kinetics. Behavior and analysis of rapid equilibrium and steady-state enzyme systems*, John Wiley & Sons, Inc., New York.
 39. Cornish-Bowden, A. (1995) *Fundamentals of Enzyme Kinetics*, Revised ed., Portland Press, London.
 40. Cleland, W. W. (1963) The kinetics of enzyme-catalyzed reactions with two or more substrates or products. III. Prediction of initial velocity and inhibition patterns by inspection. *Biochim. Biophys. Acta* 67, 188–196.
 41. Kholodenko, B. N., and Westerhoff, H. V. (1994) Control theory of one enzyme. *Biochim. Biophys. Acta* 1208, 294–305.
 42. Kacser, H., and Burns, J. A. (1995) The control of flux. *Biochem. Soc. Trans.* 23, 341–366.
 43. Brown, G. C., Westerhoff, H. V., and Kholodenko, B. N. (1996) Molecular control analysis: control within proteins and molecular processes. *J. Theor. Biol.* 182, 389–396.
 44. Diaz Ricci, J. C. (1996) Influence of phosphoenolpyruvate on the dynamic behavior of phosphofructokinase of *Escherichia coli*. *J. Theor. Biol.* 178, 145–150.
 45. Maaloe, O. (1983) *Growth of the Bacterial Cell*, (Ingraham, G. L., Maaloe, O., and Neidhardt, F. C., Eds.), Sinauer Association, Inc., Sunderland, MA.
 46. Jahn, H. A., and Teller, E. (1937) Stability of polyatomic molecules in degenerate electronic states. i. orbital degeneracy, *Proc. R. Soc. London, Ser. A* 161, 220–235.
 47. Janes, R., and Moore, E. (2004) *Metal-Ligand Bonding*, Royal Society of Chemistry.
 48. Vainer, R., Belakhov, V., Rabkin, E., Baasov, T., and Adir, N. (2005) Crystal structures of *Escherichia coli* KDO8P synthase complexes reveal the source of catalytic irreversibility. *J. Mol. Biol.* 351, 641–652.
 49. Ryde, U., Olsen, L., and Nilsson, K. (2002) Quantum chemical geometry optimizations in proteins using crystallographic raw data. *J. Comput. Chem.* 23, 1058–1070.
 50. Nielsen, J. E., and McCammon, J. A. (2003) On the evaluation and optimization of protein X-ray structures for pKa calculations. *Protein Sci.* 12, 313–326.
 51. Schutz, C. N., and Warshel, A. (2001) What are the dielectric constants of proteins and how to validate electrostatic models? *Proteins: Struct., Funct., Genetics* 44, 400–417.
 52. Parr, R. G., and Yang, W. (1989) *Density-functional Theory of Atoms and Molecules*, Vol. 16, Oxford University Press, New York.
 53. Geerlings, P., De Proft, F., and Langenaeker, W. (2003) Conceptual density functional theory. *Chem. Rev.* 103, 1793–1874.
 54. Siegbahn, P. (2006) The performance of hybrid DFT for mechanisms involving transition metal complexes in enzymes. *J. Biol. Inorg. Chem.* 11, 695–701.
 55. Jensen, K. P., Roos, B. O., and Ryde, U. (2007) Performance of density functionals for first row transition metal systems. *J. Chem. Phys.* 126, 014103–014114.
 56. Becke, A. D. (1988) Density-functional exchange-energy approximation with correct asymptotic behavior. *Phys. Rev. A: At., Mol., Opt. Phys.* 38, 3098.
 57. Vosko, S. H., Wilk, L., and Nusair, M. (1980) Accurate spin-dependent electron liquid correlation energies for local spin density calculations: a critical analysis. *Can. J. Phys.* 58, 1200–1211.
 58. Lee, C., Yang, W., and Parr, R. G. (1988) Development of the Colle-Salvetti correlation-energy formula into a functional of the electron density. *Phys. Rev. B: Condens. Matter Mater. Phys.* 37, 785.
 59. Reiher, M., Salomon, O., and Artur Hess, B. (2001) Reparameterization of hybrid functionals based on energy differences of states of different multiplicity. *Theor. Chem. Acc.* 107, 48–55.
 60. Zhao, Y., and Truhlar, D. G. (2008) Density functionals with broad applicability in chemistry. *Acc. Chem. Res.* 41, 157–167.
 61. Weinhold, F., and Landis, C. R. (2005) Perturbation theory for orbitals in the Hartree-Fock framework: the donor-acceptor paradigm., in *Valency and Bonding. A natural bond orbital donor-acceptor perspective*, Cambridge University Press, Cambridge.
 62. Hsin, K., Sheng, Y., Harding, M. M., Taylor, P., and Walkinshaw, M. D. (2008) MESPEUS: A Database of the Geometry of Metal Sites in Proteins, *J. Appl. Cryst. Allorg.* submitted.
 63. Vallee, B. L., and Williams, R. J. (1968) Metalloenzymes: the entatic nature of their active sites. *Proc. Natl. Acad. Sci. U.S.A.* 59, 498–505.
 64. Robert, J. P. W. (1995) Energised (entatic) States of Groups and of Secondary Structures in Proteins and Metalloproteins. *Eur. J. Biochem.* 234, 363–381.
 65. Gray, H. B., Malmstrom, B. G., and Williams, R. J. (2000) Copper coordination in blue proteins. *J. Biol. Inorg. Chem.* 5, 551–559.
 66. Warshel, A. (1991) *Computer modeling of chemical reactions in enzyme and solutions*, Wiley, New York.
 67. Fersht, A. (1999) *Structure and Mechanism in Protein Science: A Guide to Enzyme Catalysis and Protein Folding*, W H Freeman & Co, New York.
 68. Warshel, A., Sharma, P. K., Kato, M., Xiang, Y., Liu, H., and Olsson, M. H. (2006) Electrostatic basis for enzyme catalysis. *Chem. Rev.* 106, 3210–3235.
 69. Ryde, U., Olsson, M. H. M., Pierloot, K., and Roos, B. O. (1996) The cupric geometry of blue copper proteins is not strained. *J. Mol. Biol.* 261, 586–596.
 70. Ryde, U., Olsson, M. H., Roos, B. O., De Kerpel, J. O., and Pierloot, K. (2000) On the role of strain in blue copper proteins. *J. Biol. Inorg. Chem.* 5, 565–574.

BI801955H